Materials Today Bio 32 (2025) 101710

Contents lists available at ScienceDirect

Materials Today Bio

journal homepage: www.journals.elsevier.com/materials-today-bio

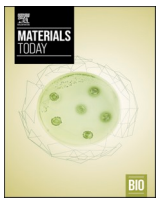

Multifunctional micro/nano-textured titanium with bactericidal, osteogenic, angiogenic and anti-inflammatory properties: Insights from *in vitro* and *in vivo* studies

Théo Ziegelmeyer [a], Karolinne Martins de Sousa [b], Tzu-Ying Liao [b], Rodolphe Lartizien [c], Alexandra Delay [a], Julien Vollaire [a,d], Véronique Josserand [a,d], Denver Linklater [e], Phuc H. Le [b], Jean-Luc Coll [a], Georges Bettega [a,c], Elena P. Ivanova [b,*], Véronique Martel-Frachet [a,f,**]

[a] *University Grenoble Alpes, INSERM U1209, CNRS UMR5309, Institute for Advanced Biosciences, F38000, Grenoble, France*
[b] *School of Science, RMIT University, Melbourne, VIC, 3000, Australia*
[c] *Service de Chirurgie Maxillo-Faciale, Centre Hospitalier Annecy Genevois, 1 Avenue de L'hôpital, Epagny Metz-Tessy, F-74370, France*
[d] *University Grenoble Alpes, INSERM U1209, CNRS UMR5309, Optimal Platform, Institute for Advanced Biosciences, 38000, Grenoble, France*
[e] *Department of Biomedical Engineering, The Graeme Clark Institute, The University of Melbourne, Parkville, VIC, 3010, Australia*
[f] *University PSL Research, EPHE, F75014, Paris, France*

A R T I C L E I N F O

Keywords:
Bioinspired mechano-bactericidal surfaces
Bone reconstruction
Titanium implants
Osseointegration
Surface topography

A B S T R A C T

Titanium (Ti) is widely used as an implantable material for bone repair in orthopedics and dentistry. However, Ti implants are vulnerable to bacterial infections, which can compromise patient recovery and lead to implant failure. While a controlled inflammatory response promotes bone regeneration, chronic inflammation caused by infections can lead to implant failure. Bone repair is a complex process in which inflammation, angiogenesis and osteogenesis are tightly interconnected, requiring cooperation between mesenchymal stem cells (MSC), macrophages and endothelial cells. Here, we fabricated bio-inspired Ti implants with either microstructured (Micro Ti) or nanostructured (Nano Ti) surface textures that exhibit robust mechano-bactericidal properties. *In vitro*, both textured surfaces improved blood coagulation and osteogenic marker expression compared to smooth Ti surfaces. Additionally, Nano Ti promoted macrophage polarization towards the M2 phenotype and enhanced the paracrine effects of MSCs on angiogenesis, key processes in tissue regeneration. *In vivo* kinetic analysis of bone reconstruction in a rat calvarial model showed that Nano Ti improved osseointegration, as evidenced by increased bone volume, mineral density, and bone-implant contact. Notably, the Micro Ti surface showed no significant differences from the control implants. These findings highlight the potential of mechano-bactericidal surface nanopatterns to simultaneously prevent infections and enhance osseointegration by modulating protein adsorption, inflammation, angiogenesis and osteogenesis. This study provides new insights into the development of bifunctional Ti implants, offering new perspectives for the next generation of implantable bone-related biomaterials.

1. Introduction

Orthopedic implants play a pivotal role in restoring skeletal integrity, functionality, and the overall quality of life of patients suffering from traumatic injuries, congenital disorders, or degenerative bone conditions. Titanium is widely regarded as an excellent material for bone implants due to its biocompatibility, strength, and corrosion resistance. However, despite advancements in the development of new

* Corresponding author.
** Corresponding author. University Grenoble Alpes, INSERM U1209, CNRS UMR5309, Institute for Advanced Biosciences, F38000, Grenoble, France.
E-mail addresses: theo.ziegelmeyer@univ-grenoble-alpes.fr (T. Ziegelmeyer), rlartizien@ch-annecygenevois.fr (R. Lartizien), ADelay@chu-grenoble.fr (A. Delay), julien.vollaire@univ-grenoble-alpes.fr (J. Vollaire), veronique.josserand@univ-grenoble-alpes.fr (V. Josserand), denver.linklater@rmit.edu.au (D. Linklater), phuc.le@rmit.edu.au (P.H. Le), jean-luc.coll@univ-grenoble-alpes.fr (J.-L. Coll), gbettega@ch-annecygenevois.fr (G. Bettega), elena.ivanova@rmit.edu.au (E.P. Ivanova), veronique.frachet@ephe.psl.eu (V. Martel-Frachet).

https://doi.org/10.1016/j.mtbio.2025.101710
Received 5 December 2024; Received in revised form 6 March 2025; Accepted 25 March 2025
Available online 27 March 2025

surgical techniques and biomaterials, titanium implants continue to pose significant risk to patients: lack of stability, local over-inflammation, and nosocomial infections are some of the challenges that highlight the need for continuous improvement of titanium biomaterials [1,2]. Implant-associated infections present a severe threat to patient recovery, frequently leading to additional medical interventions, prolonged hospitalization, and in extreme cases, implant removal [3]. Furthermore, infections trigger chronic inflammation that impairs osteogenesis and hinders efficient bone repair [4]. Therefore, it is critical to develop multifunctional biomaterials that promote bone regeneration while inhibiting bacterial colonization.

Various strategies have been investigated to confer antibacterial properties to titanium implants. One approach involves applying antibiotic-impregnated coatings (release-based coatings) or non-release coatings containing antimicrobial peptides, which act by disrupting bacterial membranes [5–7]. However, these methods face significant limitations including exhausted antibiotic release over time and the risk of antimicrobial resistance [8,9]. Other studies have investigated the antibacterial effects of nanomaterials such as copper, magnesium/zinc, or silver oxide, but the health effects of metal ion release remain unclear [10]. By contrast to chemical surface-coating methods, an emerging alternative strategy draws inspiration from nature's inherent mechanically bactericidal (mechano-bactericidal) surfaces, such as those found on insect wings, plant leaves, shark skin, and gecko feet [11–13]. Various surface modification techniques, including wet etching methods like hydrothermal synthesis and dry methods like plasma etching, and laser interference lithography, have been reported to produce bactericidal titanium surface patterns [14–19]. Investigations of the mechano-bactericidal efficacy of different pattern geometries have revealed diverse bactericidal efficacy, ranging from 5 % to 99 % toward different bacterial strains [12,20].

In the context of orthopedic or bone prosthesis surgery, the implanted material will initially interact with host biological fluid and the resultant surface-adsorption of blood proteins triggers specific cell signaling that lead to particular cellular responses [21]. For example, the blood clot formed at the bio-interface of the implanted material is rich in growth factors, cytokines and matrix metalloproteases and initiates the recruitment of innate immune cells such as neutrophils, that stimulate the release of monocyte-recruiting signals to the injury site [22]. After their recruitment, monocytes will differentiate into macrophages, which are crucial for managing inflammation at the site of injury [23]. A fine balance between inflammatory macrophages (M1) and anti-inflammatory macrophages (M2) is necessary for successful bone regeneration. Indeed, clinical study on the failure of bone implants showed that an excess of M1 macrophages around the titanium implant is an important factor related to the failure of implant materials [24]. Chemotactic factors released by macrophages at the bone defect site will induce mesenchymal stem cells (MSCs) recruitment and their differentiation into osteoblasts [25,26]. Finally, macrophages and MSC regulate angiogenesis, a crucial step during bone repair, via paracrine or juxtacrine signals [23,27]. The topography of the implant directly controls the bone defect environment. For example, cell responses including polarization of macrophages, and behavior of MSCs, including proliferation, adhesion, polarization and growth factor secretion are influenced by biomaterial topography via the transduction of mechanical cues through integrins and mechanically activated ion channels [28–35]. Therefore, the modification of surface topography is a powerful tool to influence the quality of osseointegration and, consequently, the success of the implant [29,36]. Titanium implant surface characteristics, including topography and wettability, are well known to influence macrophage attachment, activity and phenotype. However, while certain surface modifications enhance osteogenic differentiation, they can also drive macrophages toward an M1 phenotype or trigger the formation of inflammatory fibrotic capsules *in vivo* [37,38]. These effects likely stem from the host's response to the implant material, highlighting the critical role of osteoimmunomodulation in biomaterial design. Despite growing interest in mechano-bactericidal surfaces, their ability to simultaneously support osteogenesis and modulate immune responses *in vivo* remains largely unexplored.

We recently developed titanium surface modifications that exhibit two scales of surface topography (micro and nano). Although increased surface roughness typically promotes bacterial adhesion by providing more attachment sites, our uniquely designed surfaces defy this trend, exhibiting robust mechano-bactericidal properties [39,40]. Nano-patterned titanium (Nano Ti) surfaces, manufactured by alkaline hydrothermal treatment, present a dense array of sharp nanoedges of approximately 10 nm in thickness. Nano Ti induces pore formation in the membrane of attaching bacteria, leading to leakage of cytoplasmic material and bacterial cell death [41]. On the other hand, micro-patterned titanium (Micro Ti), manufactured by plasma etching, exhibits a topography composed of micropillars (3.5 μm height) that cause bacterial cell death by excessive stretching of the bacterial membrane [12]. Unlike many nanoscale surface modifications on Ti implants that require osteogenic media with supplements such as high Ca^{2+}, dexamethasone, β-glycerol phosphate, or BMP2 to induce osteogenesis *in vitro* [42], our innovative mechano-bactericidal surface patterns uniquely drive MSC adhesion, spreading, survival, and proliferation while directly promoting their osteogenic differentiation, without the need for any added growth factors. This highlights the intrinsic osteoinductive potential of our topographies, independent of exogenous biochemical stimulation.

In this study, we investigated in detail the interactions of mechano-bactericidal micro- and nanotextured titanium with the key cellular players of osseointegration. We conducted *in vitro* assessment of protein adsorption, blood coagulation, and the response of RAW 264.7 macrophages and MSCs, including expression of osteogenic markers, the paracrine effect of MSCs on angiogenesis and macrophage polarization. Furthermore, we evaluated the application of our micro-nanotextured bactericidal Ti topographies *in vivo* using a rat calvarial bone defect model, a well-established preclinical approach to assess the osteogenic potential and osseointegration of titanium implants. This model not only provides a mechanically unloaded environment, allowing precise evaluation of material-driven bone regeneration, but also enables the creation of a critical-size defect that cannot heal spontaneously, making it particularly relevant for testing bone implants [43]. We performed kinetic analysis of three parameters (bone volume, mineral density, bone/implant contact) for each rat to comparatively assess the stimulating effect on bone formation of the two Ti surface topographies. Our results demonstrate the applicability of mechano-bactericidal Ti supports as a promising solution for the development of improved, multifunctional Ti implants that combine biocompatibility, bactericidal action, osteogenic, angiogenic, and anti-inflammatory properties promoting osseointegration.

2. Materials and methods

2.1. Materials and reagents

Commercially pure (CP) ASTM Grade 2 Ti rods of 5-mm diameter were obtained from Goodfellow (Huntingdon, England). KOH pellets (85 %), absolute ethanol (99 %), and acetone (99 %) were purchased from Merck (Pty) Ltd. (Bayswater, Australia).

2.2. Preparation and surface modification of Ti

Preparation of polished Ti (Poli Ti). Commercially pure (CP) ASTM titanium rods (5-mm diameter) were obtained from Goodfellow (Huntingdon, England). A Secotom-50 instrument (Struers, Cleveland, USA) was used to cut the Ti rods into discs 1–1.5 mm thick. The Ti discs were then ground using P1200 and P2000 silicon carbide abrasive papers, then finally polished using polishing cloths (MD-Dac and MD-Chem - Struers, Australia) with 1 μm diamond paste and 0.5 μm silica colloid,

respectively. The polished Ti discs were then ultrasonically cleaned for 5 min in sequential solutions of 100 % acetone, 100 % ethanol and Milli-Q water. The various etchings made to induce a particular topography on the Ti surface were made from Poli surfaces and introduced in previous studies [39,44].

Preparation of Micro Ti. Briefly, the micron-scale topography was obtained by inductively coupled plasma assisted reactive ion etching (ICP RIE). The Poli Ti disks were placed on a quartz support within a RIE etching instrument (Plasma Lab System 100, Oxford Instruments). Etching was performed using Cl_2 gas maintained at a flow rate of 50sccm (gas flow in cm^3/min), ICP power of 1000W, RF power of 100W and pressure of 3mTorr for 40 min.

Preparation of Nano Ti. The nanoscale topography was obtained by an alkaline hydrothermal treatment. Ti discs were placed in 1M KOH for 6 h at 150 °C in a Teflon-coated autoclave. The disks were then cooled in Milli-Q water for 24 h before annealing at 450 °C for 4 h, with a temperature increase of 20 °C/min. A sonication step in ethanol 50 % for 20 min was used to remove any residual debris.

Before experimental use, the Ti surfaces were washed in PBS 0.5 % tween 20, 0.5 % Triton X-100, 1 % sodium dodecyl sulfate (SDS) under agitation for 20–30 min. Two sonication cycles were then realized (15 s ON at 90 % amplitude; 15 s OFF), the first in distilled water followed by a second in 70 % ethanol. Surfaces were then left to dry at room temperature and autoclaved.

2.3. Surface characterization

High-resolution scanning electron microscope (SEM) images of the Ti surfaces were obtained using a Nova NanoSEM 200 (FEI, Hillsboro, USA) instrument equipped with a field emission gun operated at 5 kV. The SEM images were analyzed using Image J software (version 1.48).

The surface topography of the surface was analyzed using a Nano-Wizard 4 tip scanning atomic force microscope (JPK BioAFM Business, Bruker NanoGmbH, Germany). The AFM head was positioned on a vertical optical microscope (IX81, Olympus, Japan), and the scans were performed inside an acoustic enclosure and on a vibration isolation table (Accurion, Germany). The imaging was conducted in a controlled atmosphere with air conditioning at a temperature of around 25 °C. An n-type antimony-doped silicon probe (SICON, AppNano, USA) was used in the Advanced Quantitative Imaging mode. Three scans were taken of each surface within a 5 × 5 μm^2 region, and a series of roughness parameters were then computed by using Gwyddion version 2.66.

2.4. Assessment of antibacterial performance

Gram-positive *S. aureus* CIP 65.8^T bacteria were obtained from the Collection de l'Institut Pasteur (CIP, Paris, France). Bacteria were refreshed from frozen stocks on nutrient agar (Oxoid, Thermo Fisher Scientific, Waltham, United States) for 24 h at 37 °C. Inoculating suspensions were prepared by suspending one loopful of bacteria in 5 mL of nutrient broth (Oxoid, Thermo Fisher Scientific, Waltham, United States). The cell suspensions were adjusted to an optical density of $OD_{600} = 0.1$. Sterilized Ti discs were submerged in 500 μL of bacterial suspension in a sterile 24-well plate for 18 h in a 25 °C incubator. After incubation, the samples were gently washed, stained for 25 min using a LIVE/DEAD BacLight Bacterial Viability Kit (Invitrogen, Carlsbad, United States), and imaged via CLSM (Zeiss LSM 880, Carl Zeiss Microscopy, Jena, Germany).

To further evaluate the antimicrobial activity of the coated surfaces, a modified surface antimicrobial assay was adopted based on the standard ISO 22196-2011: Measurement of antibacterial activity on plastics and other non-porous surfaces [45] The sterile Ti discs were placed in a multi-well cell culture plate with the test surfaces facing upwards. A portion of 50 μL of bacteria suspension was aliquoted onto each test surface and covered with a coverslip. The samples were incubated at 37 °C for 24 h in a humidified environment, after which the contacted surfaces were rinsed to remove non-adhered bacteria. Finally, the discs were placed in 1 mL PBS and vortexed. The wash buffer was serially diluted and spread plated on nutrient agar. Colony Forming Units (CFU) counting was performed after 24 h to determine the number of viable bacteria.

2.5. Initial biological interactions with the textured Ti

The blood was collected from rats included in the *in vivo* cranial defect study at the time of euthanasia. These experiments were carried out in replicates using blood sampled from different rats. A heparin-coated syringe (PanPharma ETI3M219-1) was used. Blood collected in this way was stored at room temperature in 1 mL heparinized tubes and used within 2 h.

For the analysis of hemolytic activity of the textured Ti, heparinized rat blood was centrifuged for 15 min at 500g, taking care to remove the brake beforehand. A solution of red blood cells was then isolated and diluted to 10 % in PBS. The Ti surfaces were immersed in this solution for 2 h at 37 °C with stirring. At the end of this incubation, the solution was collected and centrifuged at 4000g for 15 min, and 100 μL of supernatant was used to read the absorbance at 540 nm (Tecan, Sunrise). Absorbance correlates with the amount of hemoglobin released from the red blood cells. For the microscopic analysis of platelets adherence, the platelet-rich plasma was recovered and diluted 1:4 in PBS. 400 μL of this solution was applied to the titanium specimens and incubated at 37 °C for 45 min. The specimens were then washed with PBS and fixed with 4 % paraformaldehyde (PFA) for 15 min. Actin filaments were stained with phalloidin for 30 min, and fluorescence imaging was performed using a Zeiss AxioImager M2 microscope. Platelet count and spreading area were quantified using the image analysis software Cellprofiler.

The coagulant potential of the different Ti surfaces was assessed using a simple blood deposition method [46]. Blood without anticoagulant was collected intracardially using a 2 mL syringe and an 18G needle (Terumo). Within seconds, 5 μL of this blood was deposited as a drop on the surface of the titanium discs. After 15min, 30min or 45-min incubation at room temperature (ca 22 °C), 500 μL of milli-Q water was added, followed by 30 s of horizontal agitation and 5 min incubation. At the end, 200 μL of supernatant was collected for analysis at 540 nm. Absorbance correlates with the quantity of red blood cells caught in the clot.

The protein adsorption capacity of the different surfaces was assessed following a protocol inspired by Refs. [47,48]. The surfaces were incubated for 2 h in a 48-well plate on a horizontal shaker at 100 rotations per min (rpm), at 37 °C with 300 μL of a solution of either 0.2 mg mL^{-1} bovine serum albumin (BSA), 0,1 mg mL^{-1} human fibronectin or 0,1 mg mL^{-1} total rat serum. The protein solution was then aspirated and the Ti surfaces thoroughly washed 3 times with PBS. For quantification, the surfaces were then incubated for 1h at 100 rpm, 37 °C and 5 % CO2 in 200 μL of 1 % SDS. The SDS solution was then recovered and the protein it contained quantified using a protein assay kit (DC protein assay, Bio-rad). Then, protein concentration was calculated by comparing the absorbance values of our samples with a BSA standard curve.

2.6. Cell culture

MSCs derived from adipose tissue were supplied by the "Etablissement Français du Sang" of Saint Ismier (France). MSCs were cultured in mesenchymal stem cell growth medium 2 (Promocell) following the supplier's protocol. Briefly, the culture medium was changed every 3–4 days, and the cells were maintained in an environment at 37 °C and 5 % CO_2. The number of cell passages was tightly controlled, so as not to exceed 6 passages. For cell harvesting TrypLE (Thermofischer) was used, and counting was performed using a Countess automat (Invitrogen).

HUVEC cells (human umbilical cord endothelial cells) were cultured in EGM2 medium (Lonza, Colmar, France). The cells (ATCC) were used

between passage 3 and 5, and the culture medium was renewed every 2–3 days. Trypsin TrypLE (Thermofischer) was used to harvest the cells.

The RAW 264.7 macrophage cell line was purchased from American Type Culture Collection (ATCC, Manassas, United States). The cells were cultured in T75 cell culture flasks with Dulbecco's Modified Eagle Medium (DMEM, Gibco™, Life Technologies, Carlsbad, United States) at 37 °C in a humidified incubator with 5 % CO_2. The RAW 264.7 cells were sub-cultured when the cell density achieved 90 % confluency. Once confluent, the culture medium was removed, and the adherent cells were rinsed with sterile phosphate-buffered saline (PBS, Gibco™, Life Technologies, Carlsbad, United States) and trypsinized using Trypsin-EDTA (0.25 %) (Gibco™, Life Technologies, Carlsbad, United States) at 37 °C for 3 min. Then, the cell suspension was centrifuged at 250g for 5 min. Following centrifugation, the supernatant was removed, and the resultant cell pellet was resuspended in 1 mL of DMEM.

2.7. RAW 264.7 cell viability and attachment

Sterile human serum (HSP) from male AB plasma was obtained from Sigma-Aldrich (Saint Louis, United States). The Ti surfaces were immersed into 200 μL of human serum for 1 h at 37 °C. To remove unattached proteins, the samples were gently washed with PBS.

The Ti discs were placed in a sterile 96-well plate and then seeded with RAW 264.7 cells at a density of 5×10^3 cells/mL and incubated at 37 °C in a humidified atmosphere incubator with 5 % CO2. The incubation periods used for analysis were 1, 4, and 7 days.

Ti discs with attached cells were stained with calcein AM (2 μM) and ethidium homodimer-1 (4 μM) (Invitrogen, Carlsbad, United States) for 30 min under dark conditions at room temperature. The samples were subsequently imaged using confocal laser scanning microscopy (CLSM) (Zeiss LSM 880, Carl Zeiss Microscopy, Jena, Germany).

2.8. Immunocytochemistry and cytoskeleton staining

Ti discs seeded with RAW 264.7 cells were washed twice with PBS and subsequently fixed using 4 % paraformaldehyde for 15 min. The cells were permeabilized using 0.2 % Triton X-100 for a further 15 min. Following this, the cells were blocked in 1 % bovine serum albumin for 30 min. The cells were then treated with an anti-vinculin (mouse) primary antibody as an indicator of focal adhesions at room temperature for 1 h. A secondary antibody, anti-Mouse IgG in goat serum, was drop-cast onto samples and incubated for 1 h at room temperature; the actin filaments were stained using phalloidin for a further 20 min, and then the cell nuclei were stained using TO-PRO™-3 Iodide for 30 min. The cells were imaged using CLSM.

2.9. Quantification of M1 and M2 polarization markers CCR7 and CD206

Ti discs were colonized with RAW 264.7 as previously described in Section 2.7 for 2 days. After colonization, the RAW 264.7 cells were trypsinized and washed with PBS. The RAW 264.7 cells were then blocked with CD16/32 for 10 min and subsequently incubated with allophycocyanin-conjugated CCR7 and phycoerythrin-conjugated CD206 for 1 h. After incubation, the cell suspension was transferred to a 96-well plate, and the fluorescence intensity (excitation/emission: 650/660 nm for allophycocyanin and 565/578 for phycoerythrin) was recorded using a CLARIOstar Plus microplate reader (BMG LabTech Pty., Ltd., Ortenberg, Germany).

2.10. In cell ELISA assay

MSCs were seeded at 20000 cells/cm^2 onto the Ti discs (0.2 cm^2) in 96-well plates. After the desired culture period, cell viability was assessed (Prestoblue, Life Technologies SAS, Villebon, France). Ti surfaces were then fixed with 4 % paraformaldehyde (PFA) for 15 min and permeabilized with 0.2 % Triton-X100 in PBS for 15 min. Non-specific sites were blocked by incubation for 90 min with gentle agitation (20 rpm) in blocking solution (PBS 0.05 % Tween (PBST), 10 % NGS, 1 % BSA). Primary antibodies against Runx2 (Abcam, Paris, France) or Smad4 (R&D systems, Mineapolis, USA) were diluted in the blocking solution and applied to the surface of the supports for 90 min at 20 rpm. After three washes with PBST, HRP-coupled secondary antibodies were added diluted in the blocking solution for 1h. After three final washes with PBST, the signal was revealed by covering the wells with a solution of TMB (Abcam). After 15–30 min, absorbance was read at 450 nm. A semi-quantitative analysis was performed using the absorbances generated and normalizing to the previously determined cell viability.

2.11. Analysis of the composition of the extracellular matrix

An ELISA assay was performed following a previously described protocol [49]. After removing the cells by treatment with TrypLE and washing the supports thoroughly with PBS, they were incubated in a previously filtered solution of PBS, 20 mM Tris-HCl, 4 MGuHCl, 10 mM EDTA, 0.066 % (w/v) sodium dodecyl sulfate (SDS), pH 8.0. After 5 h at 37 °C, the total protein concentration in the collected sample solution was quantified using the DC protein assay kit. ELISA was performed in 96-well plates. The various extracellular matrix samples were deposited in the wells and incubated overnight at 4 °C, at a rate of 10 μg of protein per well, in a 0.05M carbonate/bicarbonate solution pH 9.6. After three washes with PBST, the wells were saturated for 2 h at 25 °C with a solution of PBS, 1 % BSA. Primary antibodies against collagen type I (Sigma-Aldrich, Saint-Quentin-Fallavier, France) or against osteopontin (Bio-techne SAS, Noyal Châtillon sur Seiche, France), diluted in PBST, 1 % BSA, were then added at a rate of 100 μL per well. After 2 h at 25 °C, the wells were washed three times with PBS 0.1 % Tween20. HRP-coupled secondary antibodies were then added diluted in PBST, 1 % BSA for 1 h. After the last three washes in PBST, the signal was revealed by adding a solution of TMB (Abcam). After 10–15 min, the plate was read at 450 nm on a Fluostar Omega instrument (BMG Labtech, Champigny sur Marne, France). To establish protein quantification, a calibration curve was prepared for each target protein studied. Briefly, the relevant wells were coated with an increasing concentration (1.25; 2.5; 5.0; 10.0; 20.0 ng mL^{-1}) of recombinant collagen type I (Thermo Fisher Scientific, Waltham, USA) or osteopontin (Biotechne).

2.12. Assessment of alkaline phosphatase (ALP) activity

After culture on our Ti surfaces, cells were recovered by adding TrypLE. After centrifugation for 5min at 250g, the cell pellet was lysed by adding 0.2 % Triton-X100 for 1 h at 4 °C. The samples were then centrifuged for 10min at 10000g to recover the protein lysate. After a protein quantification by DC protein assay, 5 μL of this lysate was used per well. The volume was made up to 80 μL with DEA 1X (Phosphatase substrate kit, Thermo Fisher Scientific). Then 50 μL of pNPP (5 mM final) dissolved in DEA 1X containing 0.5 mM MgCl2 was added to allow the reaction to proceed. Absorbance readings were taken on a microplate reader (Sunrise, Tecan, Männedorf, Switzerland) at 415 nm after 15 min, 30 min, 1 h and then 2 h. For analysis of the results, the 1 h time was used. In parallel, pNPP standards at concentrations ranging from 0 to 20nmol/well were freshly prepared and incubated with 0.2U ALP per well.

2.13. Analysis of calcium deposits

MSCs were seeded at 20,000 cells/cm^2. Cells were grown for 7–21 days, with medium replacement every 3–4 days. At the end of culture, MSCs were washed 3 times with PBS, then fixed with 4 % paraformaldehyde (PFA) for 15 min at room temperature. After removal of the PFA and washing of the cells, a volume sufficient to coat the samples with alizarin red 2 % pH 4.2 was added for 20 min at room temperature.

After three washes with distilled water, calcium deposits were quantified by dissolving the alizarin red. For this, 500 µl of a solution of 20 % methanol and 10 % acetic acid was deposited in the wells. Finally, absorbance at 450 nm was read spectrophotometrically.

2.14. MSCs conditioned medium (cmMSC)

Six days after seeding MSC (20000/cm^2), the titanium discs were transferred to new wells and 400 µl of fresh MSC culture medium with or without serum was added to the wells and incubated with the MSCs for 24 h. Conditioned media were recovered, centrifuged at 9300g for 10 min and stored at −80 °C until use.

2.15. Analysis of VEGF secretion

The cmMSC were obtained as described above. To avoid any interference from serum proteins, the conditioned medium was produced with SVF-free MSC2 medium in contact with the cells for 24 h. ELISA was performed in 96-well plates. The different cmMSC samples were diluted ½ in 0.05M carbonate/bicarbonate solution pH 9.6 to a final volume of 100 µL and incubated overnight at 4 °C. After three washes with PBST, the wells were saturated for 2 h at 25 °C with a solution of PBS 1 % BSA. Anti-VEGF primary antibody (R&D systems) diluted in PBS 0.05 % Tween 20, 1 % BSA, was then added at a rate of 100 µL per well. After 2 h at 25 °C, the wells were washed three times with PBS 0.1 % Tween20. HRP-coupled anti-mouse antibodies (Cell Signaling, Danvers, USA) were then added diluted in PBS 0.05 % Tween20, 1 % BSA for 1 h. After the last three washes with PBST, the signal was revealed by adding a solution of TMB (Abcam). After 10–15 min, the plate was read at 450 nm (Fluostar Omega, BMG Labtech).

2.16. Wound healing assay

HUVEC cells were seeded at 150000 cells/cm^2 in a 96-well culture plate. After 24–48 h, the cell monolayer was then scratched with a pipette tip. After washing with PBS to remove detached cells, 150 µL of cmMSC was added per well. The plate was then placed at 37 °C and 5 % CO2 and images of the cells invading the scratch wound were monitored for 12 h using an AxioObserver Z1 (Zeiss, Rueil Malmaison, France) associated to a MicroMAX camera (Princeton Instruments, Lisses, France) and Metamorph software (Universal Imaging, New York, USA). Quantification of wound closure was performed by image analysis using Fiji software.

2.17. HUVEC capillaries-like formation assay

The wells of a 96-well plate were coated with Matrigel with reduced growth factor level (Corning, Boulogne Billancourt, France), that was deposited in 2 successive layers of 40 µL per well, each left to polymerize for 30 min at 37 °C. HUVEC cells were then deposited on the Matrigel surface at a rate of 15,000 cells/well in 200 µL of mcCSM. The plate was then placed at 37 °C and 5 % CO2 on a videomicroscopy station (Zeiss AxioObserver Z1). Acquisitions were made every hour for 5 h. For each well, two separate fields were analyzed. Phase contrast images were analyzed with ImageJ.

2.18. Calvarial defect in vivo model

Our project and all related experimental procedures were the subject of an ethical authorization, referenced under APAFIS number #35699–202205190819354 v2. Our study was conducted on 36 male adult Wistar Han rats (Janvier Labs, Le Genest-Saint-Isle, France), aged 22 weeks (weight of 400–500g at inclusion) to exclude a potential growth effect [50]. These rats were divided into four experimental groups (Table S1, Supporting Information). The surgical procedure was performed as described by Spicer in 2012 [51], with the difference that a single 8 mm diameter implant was inserted per rat.

2.19. Micro-CT evaluation (µCT)

Rats were scanned with a µCT scanner (VivaCt, Scanco) every two weeks. Rats were positioned on the scanner bed and kept anesthetized with a mask injected with 2.5 % (vol/vol) isoflurane. X-rays were fixed at an energy of 70 keV, 114 µA and 8W. The field of view (FOV) was set at a diameter of 49.8 mm and a voxel size of 16.1 µm. The collected images were analyzed (Scanco software) by applying a contouring to the site underneath the implants (Fig. S1, Supporting Information). The bone volume per total volume sample (BV/TV) and bone densitometry (BMD) were calculated to determine the osteogenic behaviour of the implanted titanium. Visual analysis was performed on videos of the scans at times 2, 6 and 12 weeks for each rat. All µCt scan sections were exported in DICOM format and converted to avi video format using ImageJ software. Randomly generated numbers were assigned to each video. These videos were visually assessed by five examiners. Two scores were assigned by each reviewer for each video. These scores are presented in greater detail in Fig. S2, Supporting Information.

2.20. Histological analyses

The implants and surrounding tissues were collected at 12 weeks after the operation. The samples were fixed for 24 h in 4 % paraformaldehyde and stored in 70 % ethanol until used. Histological staining was performed by LLS Rowiak on undecalcified sections obtained by laser microtomy (TissueSurgeon, LLS ROWIAK GmBH, Hannover, Germany) [52]. Briefly, longitudinal sections are taken using a laser microtome at a thickness of around 10 µm. The resin covering the samples was removed to enable staining of the sections. Conventional hematoxylin/eosin (H&E) was used, with two sections stained per experimental condition.

2.21. Statistical analysis

All experiments statistically analyzed were performed a minimum of three times. Data are represented as mean ± standard deviation (SD). Statistical differences between experimental groups were tested by analysis of variance without assuming normality of distribution. Two experimental groups with a p-value of less than 0.05 were considered significantly different. Statistical analyses were performed using Graphpad Prism version 7 software.

3. Results

Micro and Nano Ti surfaces exhibit two scales of surface topography that differ in both size and shape of their surface features (Fig. 1a and b). Micro Ti was obtained by plasma etching of bulk Ti that induced the formation of high aspect ratio pillars. By contrast, the nanosheet topography of Nano Ti was obtained by hydrothermal treatment of Ti metal. Despite the different methods of surface modification, Micro and Nano Ti surfaces exhibited similar chemical composition and crystallinity (Fig. S3, Table S2, Supporting Information). However, water contact angle (WCA) measurements showed that Micro Ti exhibited increased hydrophobicity (WCA = 67.5 ± 4.5°) compared to Nano Ti (WCA = 22.0 ± 2.0°). To specifically assess the effect of topography, these surfaces were further compared to polished, non-structured titanium (Poli Ti), ensuring that material composition remained constant. The bactericidal efficacy of the two differing topographies and the Poli surface toward *S. aureus* was determined by direct quantification of non-viable cells attached to the surface via live/dead staining or by quantification of the colony forming units (CFUs) of *S. aureus* retrieved from the substratum after 24 h incubation on implant surfaces (Fig. 1c–e). Propidium iodide (PI) and Syto 9 fluorophores were used to stain the nucleic acid of viable and non-viable (membrane compromised)

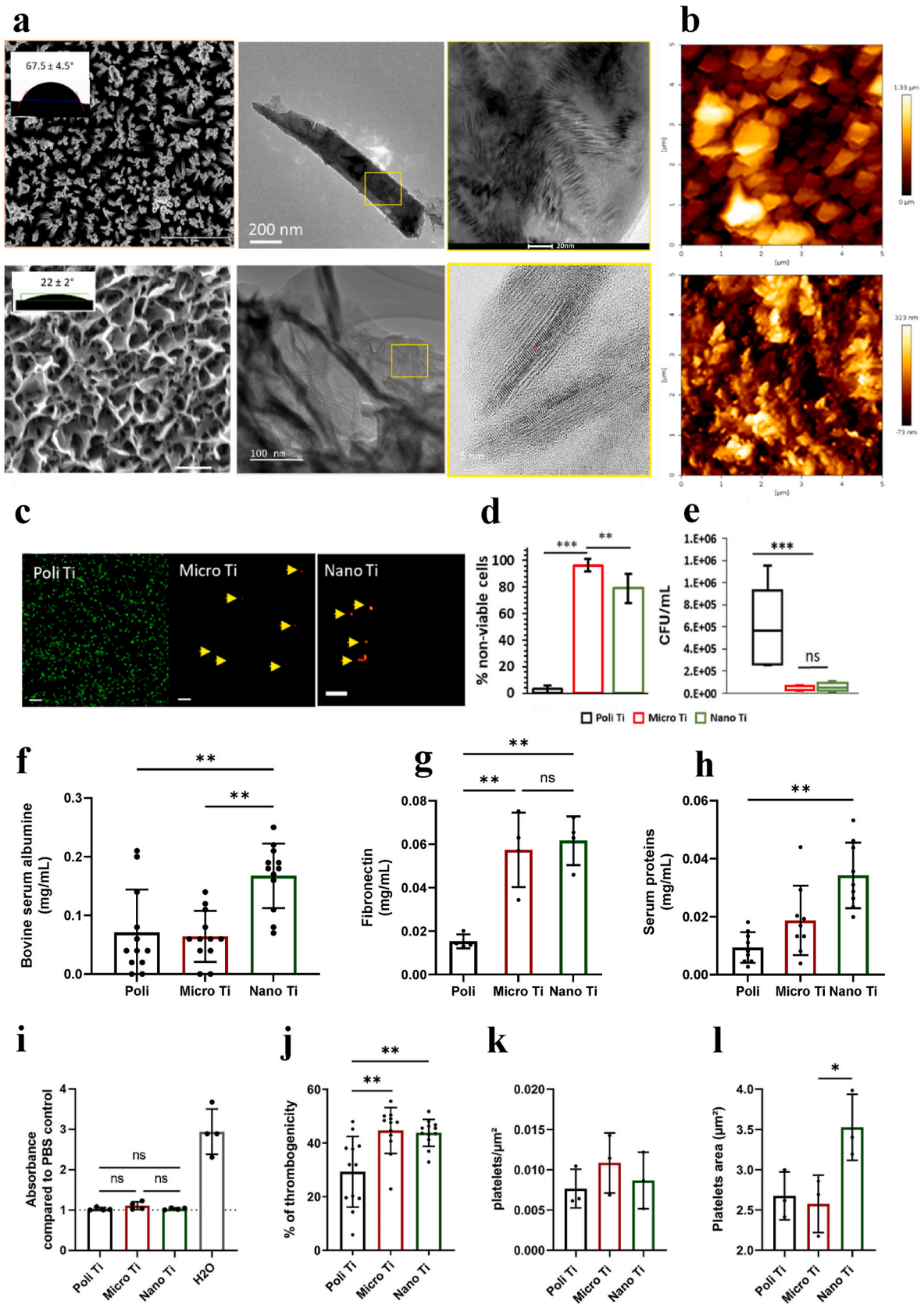

(caption on next page)

Fig. 1. Surface characterisation of Micro and Nano Ti surfaces. (a) SEM and corresponding high resolution TEM images of Ti micro-nanofeatures. Inset images show water contact angle measurements. (b) Representative 2D AFM micrograph for Micro (top) and Nano (bottom) Ti surfaces. (c–e) Antibacterial efficacy of the different Ti surfaces toward Staphylococcus aureus. (c) Representative CLSM micrographs of S. aureus attached on Poli (control), Micro, and Nano Ti surfaces, labeled with propidium iodide (red, dead cells) or Syto9 (green, live cells) fluorophores. Scale bar is 5 μm. (d) percentage of non-viable S. aureus cells derived from CLSM data. (e) Number of colony forming units (CFU) of S. aureus retrieved from the different Ti surfaces following 24 h incubation. (f–h). Quantification of protein adsorption: adsorption of bovine serum albumin (f), fibronectin (g) or serum proteins (h) by the different Ti surfaces. (i) Analysis of the thrombogenicity of the Ti surfaces. Data represent the different technical replicas for each of the biological replicas. Significance tested by one-way ANOVA test, **: p-value<0.01. (j) Quantification of hemolysis induced by our Ti surfaces. Analysis of the hemoglobin absorbance after incubation with Ti surfaces. Data are expressed as a fold change relative to the negative control, where platelets were incubated with PBS. The H2O condition corresponds to the absorbance generated following the lysis of red blood cells by osmosis with the addition of water. The experiment includes four independent biological replicates. (k) Number of adherent platelets per μm^2 after incubation for 45 min on Ti surfaces. (l) Quantification of the area of the adhered platelets. Significance tested by one-way ANOVA test, *: p-value<0.05; **: p-value<0.01; ***: p-value<0.001.

bacteria, respectively (Fig. 1c). Our results showed that 96 % and 80 % of attached S. aureus cells were considered non-viable on Micro Ti and Nano Ti surfaces, respectively, following a 24 h incubation (Fig. 1d). These data were further confirmed by the large reductions ($p < 0.001$) in CFU/mL (Fig. 1e).

3.1. Ti surface topography affects protein adsorption and platelets adhesion

During implantation, serum proteins immediately adsorb on the implant. Protein adsorption on biomaterial surfaces is a complex process influenced by several factors such as the physical properties of the surface or the conformation of the proteins. It has been reported that hydrophobic surfaces allow more proteins to adsorb [53]. However, topography also has a profound effect on protein adsorption. In general, nanostructured surfaces adsorb a greater amount of protein than smooth surfaces [10,54–56]. Nano Ti surfaces showed a significantly higher capacity to adsorb bovine serum albumin (BSA), a globular protein, compared to Micro or Poli Ti (Fig. 1f). As protein adsorption depends on the type of protein, we further assessed the adsorption of fibronectin, a fibrillar protein that plays a crucial role for cell adhesion. The amount of fibronectin adsorbed on Micro and Nano Ti was greater than Poli Ti, yet there was no statistically significant difference between the two textured Ti surfaces (Fig. 1g). To mimic the contact that occurs between blood and the implant, we also quantified the adsorption of whole serum proteins. Nano Ti exhibited significantly ($p < 0.01$) increased serum protein adsorption compared to the other types of Ti surfaces (Fig. 1h). These data suggest that Nano Ti could provide a favorable environment for cell adhesion. To further investigate this, we studied the blood contact with the different Ti topographies (Fig. 1i). There was no significant difference in hemolytic toxicity between Poli, Micro and Nano Ti, indicating that none of the mechano-bactericidal surface modifications induce the lysis of red blood cells. We also assessed the thrombogenicity of the Ti samples. As shown in Fig. 1j, Micro and Nano Ti surfaces significantly enhanced blood coagulation compared to Poli Ti. Finally, as it has been reported that platelet activation is directly linked to their adhesion, we aimed to determine whether platelets adhere differently depending on the surface [57]. Our results show no significant difference in the number of adherent platelets across the different surfaces (Fig. 1k). However, platelet spreading, a crucial step for hemostasis and wound healing, varied significantly (Fig. 1l, Fig. S4, Supporting Information). Interestingly, platelets were significantly more spread on the Nano surface compared to the Poli or Micro surfaces ($p < 0.05$). Taken together, these findings suggest that the Nano surface provides a more favorable environment for platelet adhesion, an early and critical event in bone regeneration.

3.2. Nano Ti promotes M2 macrophages polarization

Macrophages are central cells involved in the host response after a biomaterial has been implanted. Adherent macrophages on biomaterials become activated to phagocytose the biomaterial. Subsequent cytokine secretion directs the inflammatory and wound healing response to the biomaterial. Inflammation related to implanted biomaterials and potential wound healing is primarily regulated by macrophages and their polarization states [58]. Here, we evaluated the attachment of RAW 264.7 macrophages to the Ti surfaces with or without human serum protein (HSP), mimicking the layer effect (Fig. 2a). RAW 264.7 macrophage cells colonized Poli, Micro, and Nano Ti surfaces to a similar degree on day 1; however, at longer incubation times, RAW 264.7 cells were unable to proliferate on the Micro Ti and were no longer detectable after 7 days (Fig. 2b). Then, the viability of RAW 264.7 cells after incubation with the Ti surfaces was assessed after 1-, 4-, and 7-days. Nano and Poli Ti surfaces showed no obvious cytotoxicity to the RAW 264.7 cells, with cell viability greater than 90 % (Fig. 2c). In contrast, a significantly increased number of dead cells were observed on the Micro Ti surfaces compared to the Poli Ti control and Nano Ti surfaces. Indeed, the viability of RAW 264.7 cells on the Micro Ti surfaces was approximately 40 % on day 1. The addition of an adsorbed serum protein layer improved macrophage viability to 75 %. On day 4, the viability of RAW 264.7 cells on the Micro Ti surfaces and Micro Ti with serum proteins was below 20 % and 50 %, respectively. These data suggest a low cytocompatibility of the Micro Ti surfaces with RAW 264.7 macrophages which could be detrimental to ensuring proper osseointegration of the implant.

The cytoskeletal changes of the macrophages after encountering the Nano Ti surfaces were evaluated by fluorescence microscopy after 2 days of incubation (Fig. S5, Supporting Information). The RAW 264.7 cells cultured on Nano Ti presented a significantly enhanced cell area when compared to the Poli surfaces, with 149.3 ± 32.1 and 154.7 ± 28.9 μm^2 for Nano Ti and Nano Ti + HSP; and 112.7 ± 15.4 and 120 ± 25.8 μm^2 for Poli Ti and Poli Ti + HSP, respectively (Fig. S5b, Supporting Information). Quantification of focal adhesions via vinculin staining revealed significantly greater numbers of focal adhesion sites for macrophages cultured on Nano Ti surfaces compared to Poli Ti. This effect is particularly pronounced on Nano Ti surfaces conditioned with HSP, with 42.3 ± 9.5, 54.9 ± 10.2, 83.4 ± 7.5, and 103.7 ± 12.8 focal adhesions per cell for Poli Ti, Poli Ti + HSP, Nano Ti, and Nano Ti + HSP, respectively (Fig. S5c, Supporting Information). No significant differences were found between the investigated surfaces for cell aspect ratio and nuclei area (Figs. S5d–e, Supporting Information). The cytoskeletal morphology of RAW 264.7 cells in response to the Micro Ti surfaces exhibited irregular nuclear morphology. Additionally, the actin filaments were found to be fragmented. These results indicated that the macrophages on the Micro Ti surfaces did not exhibit a clearly defined or intact shape, pointing towards the possibility of cell death at this stage (data not shown).

Classically activated (M1) macrophages upregulate pro-inflammatory cytokines, inhibit anti-inflammatory cytokines, and produce nitric oxide. Pro-inflammatory M1 macrophages generally express surface markers CD86 and CCR7. Over time, biomaterial-adhered macrophages switch to the type 2 (M2) phenotype, which is associated with the expression of anti-inflammatory cytokines to reduce inflammation and initiate tissue repair and wound healing. Anti-inflammatory M2 macrophages produce high levels of ARG1 and IL-10 with surface markers CD163 and CD206 [59,60]. The presence of a greater

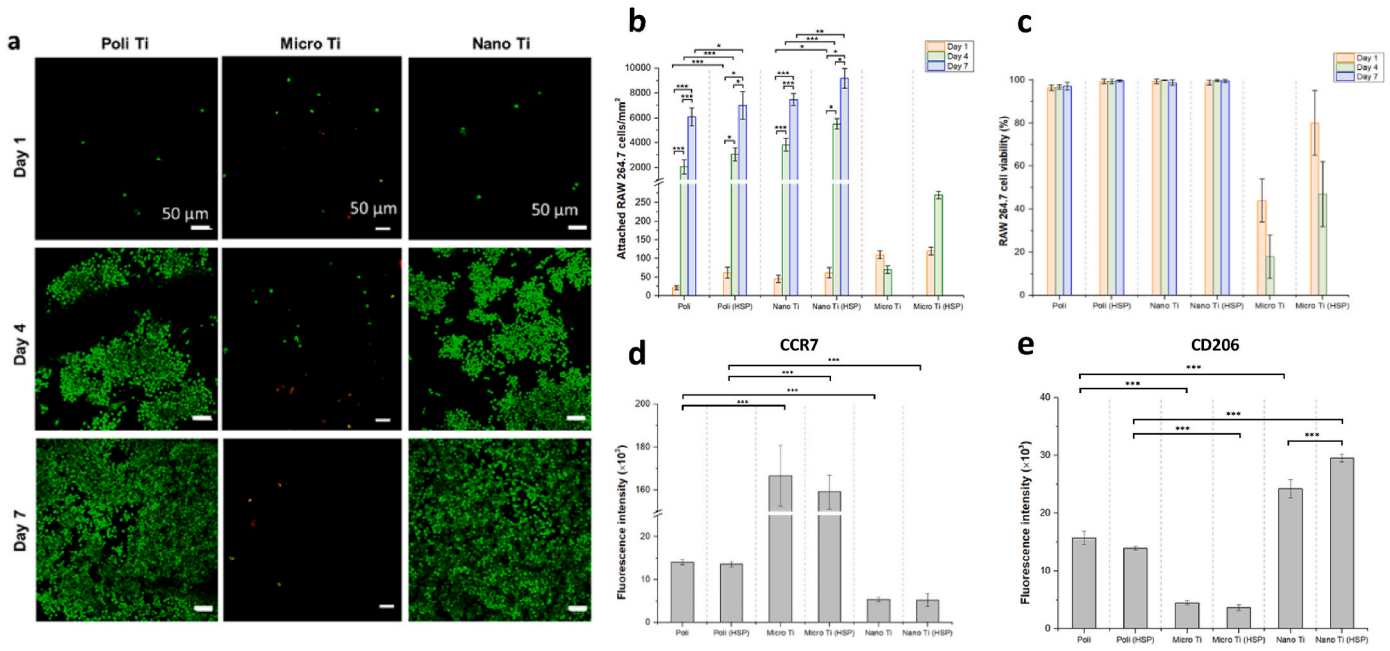

Fig. 2. RAW 264.7 cell adhesion on Ti surfaces. (a) Representative CLSM micrographs of attached cells on Ti surfaces. Scale bar = 50 µm. (b) Macrophage cell density expressed as the number of attached RAW 264.7 cells per mm^2 (c). Macrophage cell viability in contact with textured Ti surfaces before and after protein adsorption. Cells were stained with calcein AM (green live cells) and ethidium homodimer (red dead cells). Macrophage polarization as determined by M1 and M2 biomarkers (d) CCR7 and (e) CD206 after 2 days of incubation on the Ti surfaces. Statically significant differences are labeled as *: $p < 0.05$; **: $p < 0.01$; ***: $p < 0.001$.

proportion of M1 to M2 macrophages is highly indicative of implant failure as a chronic foreign body response elicited by M1 macrophages impairs osseointegration. Therefore, the polarization state of RAW 264.7 cells on the Micro and Nano Ti surfaces were also assessed via the quantification of the M1-and M2-type biomarkers (CCR7 and CD206, respectively) after 2 days of incubation (Fig. 2d and e). The cells on the Nano Ti surfaces exhibited a down regulated level of CCR7 compared to that on the Poli Ti and Micro Ti surfaces, indicating a potential shift away from the M1 pro-inflammatory phenotype. Instead, the RAW 264.7 cells exhibited a significantly enhanced level of CD206, which is indicative for development of M2 phenotype to enhance osseointegration. It is worth noting that serum protein adsorption was determined to be a prerequisite for enhancing macrophage response to Nano Ti surfaces. In contrast, RAW 264.7 cells exhibited a poor cell attachment to Micro Ti surfaces, associated with a high cell death rate, and induced polarization toward pro-inflammatory M1 phenotype. The anti-inflammatory response of RAW 264.7 cells on Nano Ti was further confirmed using RT-qPCR (Fig. S6, Supporting Information).

3.3. Micro Ti and nano Ti promotes in vitro osteogenic differentiation of MSCs

Protein adsorption, blood clot formation, and the inflammatory response are the initial events required for osseointegration. Then, MSCs are recruited, adhere to the surface of the implant and differentiate into osteoblasts. As shown in Fig. 3a–c, both Micro and Nano Ti surfaces allowed MSC attachment and proliferation.

The relevant expression levels of two transcription factors, Runx2 (runt-related transcription factor 2) and Smad4, were quantified as early biomarkers of osteogenic differentiation of MSCs on the Ti surfaces. These two proteins are considered as contributors to osteoinduction by micro/nano-topographies. Runx2 plays a key role as a transcription factor for a multitude of osteogenic genes but its association with Smad4 is necessary to transduce BMP stimulus as an osteogenic signal leading to the differentiation of MSC into osteoblasts [61,62]. As shown in Fig. 3d, both Micro and Nano Ti surfaces significantly enhanced the protein expression of Smad4 by MSCs after 5 days compared to Poli Ti. It should be noted that Micro Ti appears to most efficiently stimulate the amount of Smad4 compared to Nano Ti, since we observed 2 × more Smad4 on Micro Ti surfaces and 1.5 × more Smad4 on Nano Ti surfaces than on Poli Ti, respectively. For Runx2, we observed a slight, but non-significant, increase in expression after 5 days on the Nano Ti surfaces, which appears also on Micro Ti at 7 days (Fig. 3e).

To further clarify the osteogenic differentiation of MSCs on the Ti surfaces, we analyzed the amount of two other markers of osteogenic differentiation, collagen I and osteopontin. The secretion of collagen I is essential to the formation of bone matrix and contributes to the differentiation of MSCs [63] whereas osteopontin is a late-stage marker of osteogenic differentiation [64]. After extraction of the extracellular matrix produced by the MSCs, collagen I was quantified by an ELISA assay. Our data showed that both Micro and Nano Ti surfaces stimulate a greater secretion of collagen I by attached MSCs in comparison to Poli Ti (Fig. 3f and g). However, there was no significant difference between Micro and Nano Ti surfaces. At 7 days, there was an increase of osteopontin secretion on the two textured Ti surfaces compared to Poli Ti, but the difference did not reach statistical significance (Fig. 3h). This increase in osteopontin secretion persists at 14 days (Fig. 3i).

Overall, our *in vitro* studies on MSCs suggest that both types of mechano-bactericidal Ti surface patterns enhance osteogenic differentiation to a greater extent than Poli Ti but with comparable efficiency.

3.4. Nano Ti enhances secretion of pro-angiogenic paracrine signals by MSCs

Several groups have shown that bone repair is regulated through paracrine signals between MSCs and local endothelial cells [65,66]. To determine if the different Ti topographies could affect the factors secreted by MSCs, we collected the media conditioned by MSCs (cmMSC) after 7 days of culture on the textured Ti surfaces (Fig. 4a). As MSCs promote angiogenesis by secreting vascular endothelial growth factor (VEGF), we analyzed the amount of VEGF in the different cmMSC. Both Micro and Nano Ti significantly ($p < 0.05$ and $p < 0.0005$ respectively) enhanced the secretion of VEGF by MSC compared to Poli Ti (Fig. 4b). However, this increase was notably greater with Nano Ti (p

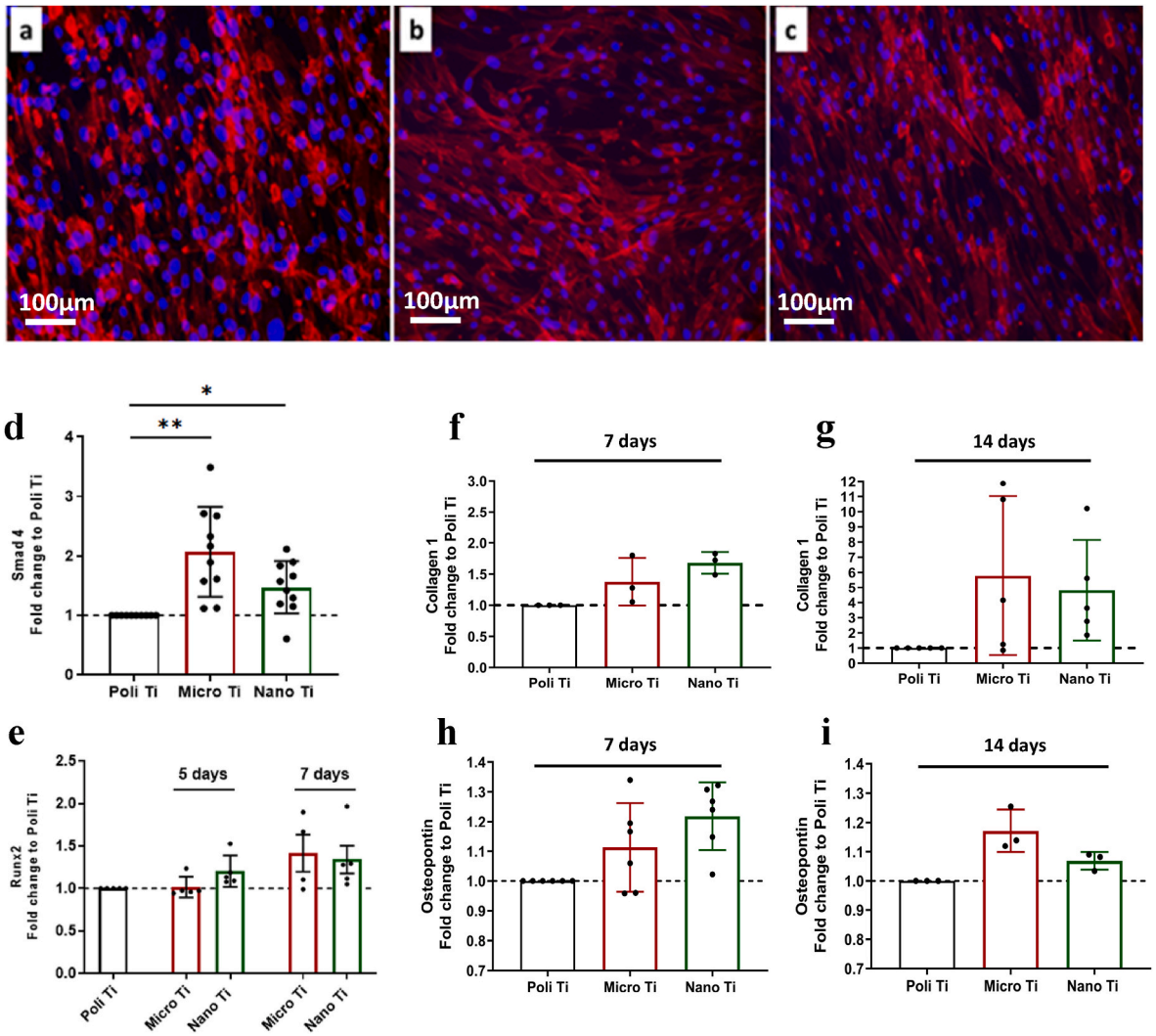

Fig. 3. Nano Ti promotes *in vitro* osteogenic differentiation of MSCs. (a–c) Confocal laser scanning micrographs of MSC proliferation on Poli Ti (a), Micro Ti (b) or Nano Ti (c) surfaces after 4 days; nuclei (blue), f-actin (red). (d, e) Quantification of Smad4 (d) and Runx2 (e) by in-cell ELISA after 5 days (d, e) or 7 days (e) of culture on the different titanium surfaces. The values represent the signal intensity of the immunostaining normalized to the number of viable cells and expressed as a fold change relative to Poli Ti. The data derived from 4 independent experiments. Each point represents a technical replica. (f–i) Evaluation of collagen 1 (f–g) and osteopontin (h, i) secreted into the extracellular matrix by MSCs on different Ti after 7 days (f, h) or 14 days (g, i). The data represent the mean ± SD of the fold change relative to Poli Ti, based on a minimum of 4 independent experiments. Statistical analysis was performed using Friedman test, **: p-value<0.01; *: p-value<0.05.

< 0,0005) than with Micro Ti ($p < 0,05$), with a 2-fold and 1.6-fold increase respectively. These results prompted us to determine the potential paracrine action of MSCs cultured on micro/nano-textured Ti on angiogenesis. First, we analyze the proliferation of HUVEC grown in these conditioned media. We did not observe any difference between the different conditions (data not shown). Then, a wound-healing assay was performed to analyze the impact of cmMSC on HUVEC endothelial cells migration, an essential step toward angiogenesis (Fig. 4c). cmMSC from cells incubated on Poli or Micro Ti have almost the same effect on HUVEC migration (Fig. 4d). However, cmMSC from MSCs grown on Nano Ti significantly enhanced the migration ability of HUVEC cells, with an increase of 1.4-fold compared to cmMSC obtained on Poli Ti. Finally, we analyzed the effect of cmMSC on the *in vitro* capillary network organization of HUVECs on Matrigel. After an incubation of 6h, microscopic observation revealed that cmMSC from Nano Ti significantly enhanced the organization of a network structure compared to Poli or Micro Ti, as demonstrated by the quantification of the number of nodes or total segment length (Fig. 4e–g). Altogether, our data demonstrate that Nano Ti enhanced the secretion of angiogenic paracrine factors by MSCs, which would be indicative of successful osseointegration.

3.5. Nano Ti enhances osseointegration in vivo

Micro and Nano Ti are osteoinductive surfaces, since they induce osteogenic differentiation of MSCs without the need of osteogenic growth factor. However, Nano Ti appears better suited to enhance osseointegration by promoting macrophage adhesion and polarization towards an M2 phenotype. Additionally, Nano Ti stimulates the secretion of proangiogenic factors. Therefore, the potential of Micro and Nano Ti surfaces as new implants for bone repair was assessed using a rat calvarial defect model (Fig. 5a). This model allows the establishment of a uniform, reproducible and standardized defect that is easily accessible for radiographic analysis. Furthermore, the dura and the overlaying skin represent an adequate support for implanted materials, without the need for internal or external fixation [67]. In order to analyze the osseointegration of the Ti biomaterials, it was necessary to create a critical size defect that could not be spontaneously repaired by the host organism

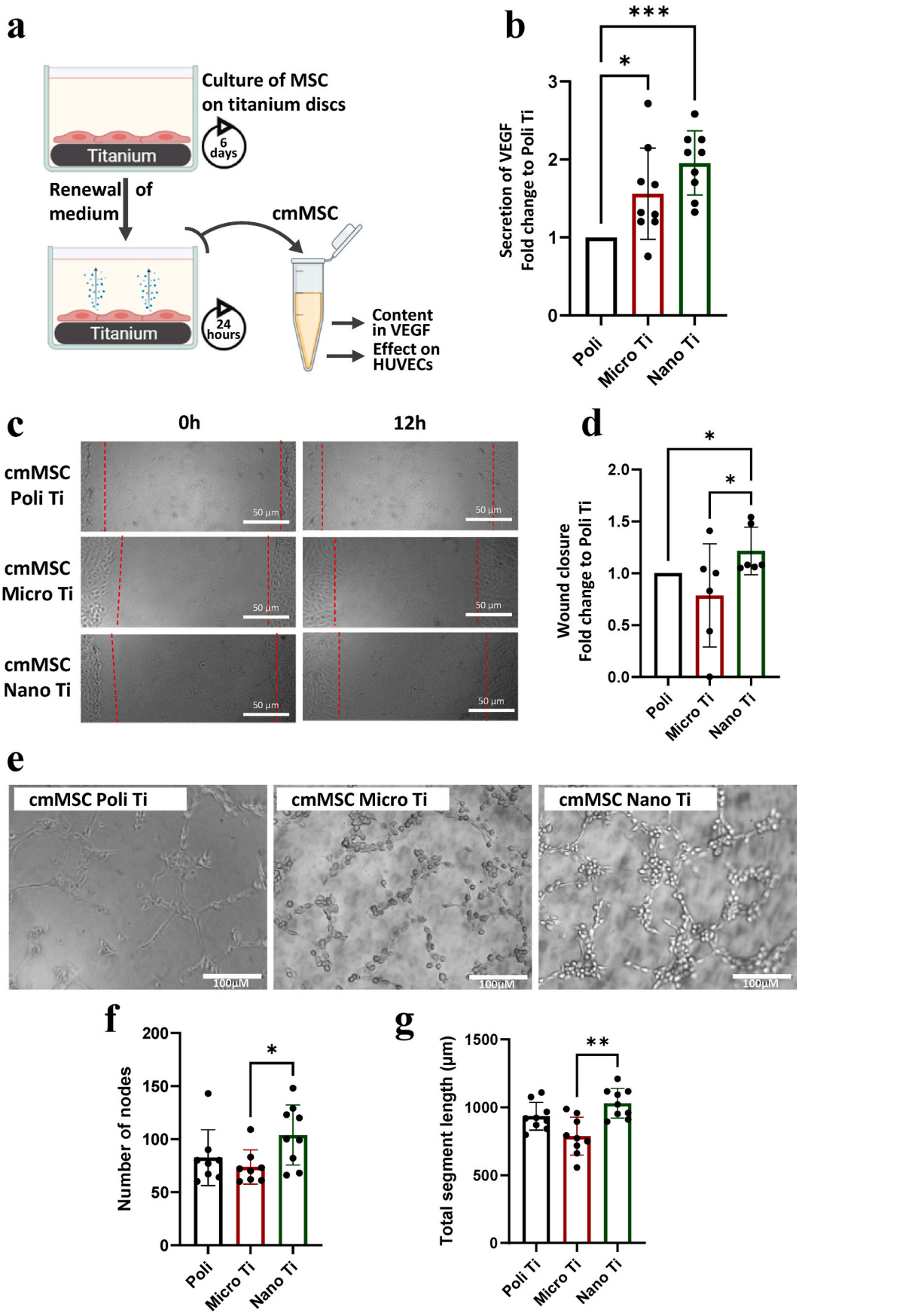

(caption on next page)

Fig. 4. Effects of MSCs-secreted paracrine factors on endothelial cells. (a) Schematic representation of the preparation of conditioned medium from MSCs (cmMSC). (b) Analysis of secreted VEGF in cmMSC by ELISA assay. The data show the amount of VEGF secreted by MSCs, normalized to the number of viable cells and expressed relative to the Poli Ti condition. (c) Representative images of the wound-healing assay on HUVECs incubated for 12 h with cmMSC obtained from MSC cultured on different Ti surfaces for 7 days. (d) Quantified results of the wound healing assay. (e) Representative images of the *in vitro* Matrigel angiogenesis assay. HUVECs were incubated with cmMSC from MSCs cultured on different Ti surfaces for 7 days. (f) Tube-forming ability was quantified by the number of nodes and the total length of segments determined through Image J analysis. All data are presented as the mean ± standard deviation of three independent experiments. In each experiment, a different cmMSC was tested in duplicate. Significance tested by Kruskal-Wallis test, ***: $p < 0{,}0005$; **: $p < 0{,}005$; *: $p < 0{,}05$.

[68]. An 8 mm defect is considered to be the most relevant [69]. This was confirmed by the controls without implant whereby the defect remained unhealed until 12 weeks after surgery (Fig. S7a, Supporting Information). After implantation of the different Ti surfaces (Micro, Nano and Poli), bone regeneration was observed by micro-CT every 2 weeks until 12 weeks after surgery (Fig. S7b, Supporting Information). There was no significant decrease in the weight of any of the animals, indicating unchanged feeding behavior after implantation of the Ti implants (Fig. S7c, Supporting Information). The bone volume fraction (BV/TV) was monitored from high resolution micro-CT analysis. This ratio increased significantly over time with Nano Ti compared to Poli or Micro Ti supports (Fig. 5b). The difference in BV/TV was visible as early as 6 weeks after surgery. In the case of Nano Ti, we observed approximately 3.2 times more bone volume at 12 weeks than at 2 weeks. The same result was obtained when we analyzed the bone mineral density (BMD). A significant increase in BMD was visible for Nano Ti implants compared with Poli and Micro Ti at 8, 10 and 12 weeks (Fig. S8, Supporting Information). A visual assessment of bone formation (Fig. 5c) confirmed the increase in bone formation surrounding Nano Ti implants was apparent as early as 2 weeks after surgery and became significantly greater after 6 weeks compared to Micro or Poli Ti implants. The visual assessment method enabled us to assess the quality of the contact of the newly formed bone with the implant. Indeed, the metal artefact present on the micro-CT images prevents a proper quantification of this parameter on scans [70]. After 12 weeks, the average score derived from visual assessment of bone formation on rats implanted with Nano Ti was 2.6 ± 0.9, which indicates the presence of newly formed bone from the implant periphery towards the center of the implant. Interestingly, visual analysis of the images confirms that the Nano surface promotes the formation of new bone tissue in direct contact with the implant (Fig. 5d). These findings highlight a significant difference between the Nano Ti surface and the other two surfaces (Poli Ti and Micro Ti).

Importantly, in the case of Micro Ti, we noticed the presence of "non-responding" rats that means that no bone formation was apparent even after 12 weeks of implantation. The number of non-responding rats was 4 out of 10 rats with Micro Ti (Table S3, Supporting Information). Comparatively, 2 out of 10 rats implanted with Poli Ti were non-responders. In contrast, all the Nano Ti implants promoted bone formation.

A qualitative histological evaluation (Fig. 5e) was used to confirm the visual assessment of bone formation. As expected, a greater amount of newly formed bone tissue was observed on Nano Ti implants, as indicated by the presence of the large area of dark pink coloration. This bone appears mature, as confirmed by the presence of highly cellularized tissue containing adipocytes representative of hematopoietic tissue. Furthermore, Nano Ti promotes bone formation over the entire implant surface, in line with the visual score established on the micro-CT images. On the other hand, Micro Ti implants do not appear to improve the ability of smooth titanium (Poli Ti) to promote osteogenesis, since the amount of newly formed bone seems similar with Micro or Poli Ti. It should be noted that a thin layer of non-bony tissue, as indicated by its pale pink coloration, appears between the bone and the Poli Ti implant. This suggests the formation of connective tissue, which could be indicative of fibrosis and poor osseointegration. *In vivo* assessment of the textured Ti implants showed that Nano Ti clearly promotes the osseointegration of the implant compared to Micro and Poli Ti. Micro-CT and histological analysis suggest that Nano Ti surfaces significantly increased the amount and rate of bone formation compared to Micro and Poli Ti. Furthermore, this formation of new bone occurs on the entire surface of the implant, without the formation of connective tissue, indicating a successful osseointegration.

4. Discussion and conclusions

The success of orthopedic, dental or maxillofacial implants is generally limited by the risk of implant-related infections and a lack of integration at the bone-implant interface. An efficient biomaterial must not only serve as a physical support but also be bioactive towards bacteria and host tissues to ensure safe and successful implantation. Despite the increasing number of publications on the development of biomaterials for bone repair, only a limited number of bone substitutes are clinically available [71]. Previously, we developed Ti surfaces with a bioinspired topography that prevent bacterial infection by killing contacting bacterial cells via a biophysical mechanism [39]. While it is well known that implant surface topography influences biomaterial-host tissue interactions, the impact of mechano-bactericidal Ti topographies on key players involved in osseointegration remains unclear [72–75]. In this study, we compared the osseointegration of Ti implants with microtextured or nanotextured surfaces with a non-textured, smooth Ti surface. Both Micro and Nano Ti topographies, known to have mechano-bactericidal properties and the ability to induce osteogenesis *in vitro* [39], were evaluated to simulate the cascade of events occurring during bone implant grafting.

Surface topography and wettability play a crucial role in protein adsorption, a key initial step in bone repair. Both Micro and Nano Ti significantly enhanced the adsorption of proteins such as BSA and fibronectin compared to a smooth surface. This is likely due to the increased surface area available for protein binding onto these textured surfaces. Nano Ti, in particular, promoted protein adsorption to a greater degree, potentially creating a more favorable environment for cell adhesion and immune response modulation. For instance, adsorption of fibronectin is essential for the initial adhesion and spreading of osteoblasts-like cells [76], and adsorption of albumin enhances the expression of anti-inflammatory cytokines by macrophages [77]. Moreover, the adsorption of fibronectin can participate in increasing platelet adhesion and activation. This could correlate with the improved thrombogenesis observed on Nano Ti surfaces. Indeed, this is in accordance with studies linking the presence of nanotopographies on the surface of implants and an increase in platelets activation, blood clot formation and the release of factors such as PDGF and TGFβ [31,78,79]. As a result, it will likely create a conducive environment for the recruitment of MSC, endothelial cells and immune cells to promote bone formation. These cells will further interact with these topographies.

Macrophages are sensitive to mechanical information from surface topography that influences their polarization and can control the macrophage-secreted cytokines and chemokines [80–84]. Macrophages sense surface topography via integrin receptors, which cluster into focal adhesion complexes, transmitting mechanical stimuli to the nucleus and promoting osteogenic gene expression [85,86]. Recent work to characterize macrophage response to disordered nanotopography on ZrOx surface indicates a reduction in macrophage stiffness, as measured by the Young's modulus, in response to the nanostructured surface. The authors found that the mechanical signals from the substrate are transmitted into the cell through integrin-mediated focal adhesions and cytoskeletal rearrangements, which ultimately reduce cell stiffness. The surface nanotopography and the resulting biomechanical changes

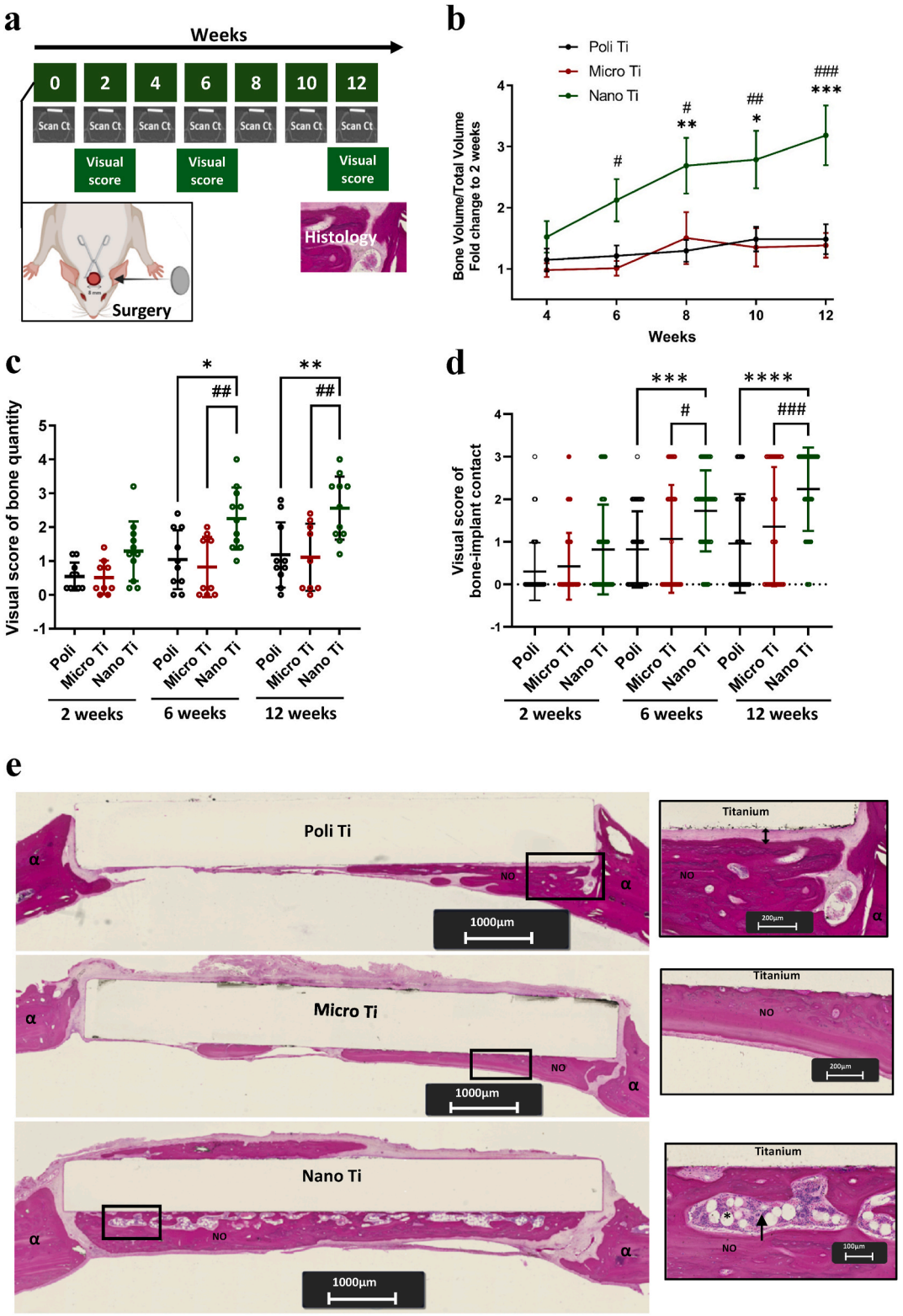

Fig. 5. In vivo evaluation of bone formation and osseointegration. (a) Schematic of the defect model. For each condition, the number of rats was as follows: Poli: 10 rats; Micro Ti: 10 rats; Nano Ti: 12 rats. (b) Evolution of the quantity of newly-formed bone in contact with the implant. BV/TV (BV, bone volume; TV, total volume). Values are expressed relative to the 2-week value for each individual. Data are presented as mean ± SD. (c) Visual assessment of the amount of newly formed bone according to the topography on the titanium implant surface (score 0: no bone formation; score 5: the newly-formed bone covers almost completely the implant surface). Data are presented as mean ± SD of scores established by 5 evaluators. (d) Visual assessment of newly formed bone in direct contact with the implant. Each point represents a visual score (score 0: no contact; score 3: full contact between new bone and implant). Data are presented as mean ± SD of scores established by 5 evaluators. (e) Hematoxylin-eosin staining of implant sections 12 weeks after *in vivo* implantation. From top to bottom, Poli, 2T and HTE implant. Host bone is observed at both ends of the implant (α). The black boxes on the right correspond to a slightly enlarged area. NO: newly formed bone; *: Adipocytes; →: hematopoietic tissue, characteristic of bone marrow; ↔: tissue interposed between the bone and the implant. The p-value was calculated by 2way ANOVA test, ***:p-value<0.0005; **:p-value<0.01; *:p-value<0.05 between Poli and Nano Ti. ###:p-value<0.0005; ##:p-value<0.01; #:p-value<0.05 between Micro and Nano Ti.

influence macrophage behavior by enhancing their mobility and phagocytic capacity, without notably affecting their inflammatory response [87]. Generally, the response of macrophages to TiO_2 nanotube surfaces demonstrates that small nanoscale features (<80 nm) are more effective in facilitating M2 polarization than non-structured/polished titanium surfaces and surfaces containing larger nanotubes. Nevertheless, it is worth noting that nanotubes with a diameter of 90 nm have also been observed to induce M2 polarization in RAW 264.7 macrophage cells [83]. The influence of other nanoscale architectures on macrophage polarization, such as nanowires or nanosheets, has not been clearly defined, generating conflicting results [88–90] (Table S4, Supporting Information). Li and colleagues reported Ti nanowires with increased cell area influenced macrophage polarization toward the M2 phenotype. By contrast, a study of macrophage response to hydrothermally etched Ti nanowires with different aspect ratios, and hence different elastic moduli, showed that nanostructures with low elastic moduli contribute to enhanced cell spreading and polarization toward the M1 phenotype, whereas nanostructures with high elastic moduli are not advantageous to macrophage spreading and result in a decreased immune response [91]. Interestingly, here, the Nano Ti topography induced a greater spreading of attached macrophages and their polarization towards the M2 phenotype. This aligns with our previous study demonstrating that, on nanostructured Ti surfaces infected with *S. aureus*, macrophages exhibited wound healing behavior with superior activation of M2-like macrophage polarization and secretion of anti-inflammatory cytokines. By contrast, macrophages attached to infected smooth surfaces activated the M1-like polarized phenotype via the high expression of pro-inflammatory cytokines, indicating persistent inflammation [92]. Therefore, Ti nanostructures created by an alkaline etching treatment can promote macrophage attachment and proliferation and tune macrophage polarization toward a M2-like phenotype [93–95]. By contrast, the Micro Ti topography favored strong CCR7 expression, indicating an M1 phenotype. However, unlike the Poli Ti which is conducive to cell adhesion and proliferation and favors the M1 phenotype, the Micro Ti condition was not suitable to macrophage attachment and proliferation.

It is well documented that surface topography regulates MSC adhesion, proliferation, and osteogenic differentiation, along with matrix secretion and mineralization [96–98]. It has been shown that controlled nanotopography can guide osteogenic differentiation of MSCs without osteogenic supplements [96]. Herein, both Micro and Nano topographies appeared to be osteoinductive, as evidenced by the increase in various markers in the differentiation timeline. Furthermore, Ti-based implants often face poor early vascularization, which can be a critical factor for successful osseointegration. However certain surface modifications can enhance angiogenesis and directly improve bone-implant integration [99]. MSCs are known to secrete VEGF, that primarily acts on endothelial cells, regulating their proliferation and migration. We observed a significant increase in VEGF secretion by MSCs attached on Nano Ti compared to Poli Ti, likely influenced by the topographical cues perceived by MSCs. In response to conditioned media from MSCs cultured on Nano Ti, HUVEC cells exhibited enhanced migration and tube formation in Matrigel. Conversely, on Micro Ti, where VEGF secretion was not significantly different from Poli Ti and no significant pro-angiogenic effect was observed. These findings suggest that the presence of nanostructures on titanium could play a crucial role in promoting vascularization of the defect *in vivo* and would need to be validated to confirm their relevance and applicability in more complex biological conditions.

Effective bone repair requires balanced osteoimmunomodulation, characterized by an initial phase of inflammation, followed by a transition of macrophage polarization to an M2 phenotype that reduces inflammation and facilitates tissue regeneration. A prolonged M1 polarization can prevent osseointegration [100]. A question remains concerning the inadequacy of Micro Ti to promote macrophage adhesion and viability, despite its ability to induce MSCs osteogenesis. The differential responses of macrophages and MSCs to the Micro Ti topography may be attributed to differences in cell size and elasticity. A study on progenitor neural stem cells demonstrated that increasing the aspect ratio and size of surface features from the nano-to micro scale confines cell morphology, leading to significant cytoplasmic penetrations and nuclear deformation [101]. Similarly, an array of micropillars with heights >3 μm significantly decreased epithelial cell adhesion and spreading [102]. This suggests that while the larger size of MSCs allows them to adapt to Micro Ti, the smaller size and lower elasticity of macrophages hinder their ability to adhere and function properly. Ultimately, Micro Ti appears unsuitable for bone repair despite its *in vitro* osteogenic potential. Thus, the poor *in vivo* performance of Micro Ti observed in this study may stem from the inability of the high aspect ratio surface features to support macrophage attachment and proliferation. This could eventually result in an inadequate macrophage response, including a lack of osteogenic factors such as BMP2 and TGF-β [103]. By contrast, Nano Ti provided a favorable environment for macrophage attachment and M2 polarization, which correlated with enhanced bone formation and bone-implant contact *in vivo*. Histological analysis at 12 weeks confirmed the presence of adequate bone production, likely deposited through contact osteogenesis, with apparent maturation evidenced by the presence of bone marrow.

Addressing the dual challenges of osseointegration and infection prevention is crucial given the increasing demand for Ti implants. Our study demonstrates the efficacy of a novel multifunctional nanotextured Ti surface that successfully meets both requirements. Hydrothermal treatment of titanium is a well-established and widely recognized technique. It is cost-effective and adaptable to various implant sizes, including porous 3D implants. However, we believe that with optimized protocols, its potential extends far beyond current applications. Notably, few studies have explored the mechano-bactericidal activity of surfaces treated using this approach. Research on bactericidal and osseointegrative surfaces often results in highly bioactive innovations, but these approaches are frequently difficult to industrialize due to complex treatment steps [94,104] or the need for external activation methods, such as titanium scaffolds activated by near-infrared irradiation to achieve antimicrobial activity [105]. In contrast, Nano Ti stands out due to the simplicity of its treatment process, which imparts a range of bioactive properties while remaining scalable for industrial production, making it a practical and innovative solution.

In conclusion, this nanostructured Ti surface, produced by alkaline hydrothermal etching, represents a promising strategy for the development of bifunctional bone implants that combine antimicrobial activity with enhanced osseointegration. Its nanotextured surface fosters a favorable immune response, supports vascularization and promotes bone formation, making it a clinically relevant strategy for improving Ti-based implants.

CRediT authorship contribution statement

Théo Ziegelmeyer: Writing – original draft, Methodology, Investigation, Formal analysis, Data curation. **Karolinne Martins de Sousa:** Methodology. **Tzu-Ying Liao:** Methodology, Formal analysis. **Rodolphe Lartizien:** Methodology, Investigation. **Alexandra Delay:** Investigation. **Julien Vollaire:** Investigation. **Véronique Josserand:** Methodology. **Denver Linklater:** Writing – review & editing, Visualization, Methodology, Investigation. **Phuc H. Le:** Visualization, Methodology. **Jean-Luc Coll:** Writing – review & editing. **Georges Bettega:** Methodology, Investigation. **Elena P. Ivanova:** Writing – review & editing, Supervision, Conceptualization. **Véronique Martel-Frachet:** Writing – original draft, Supervision, Project administration, Methodology, Funding acquisition, Conceptualization.

Declaration of competing interest

The authors declare that they have no known competing financial

interests or personal relationships that could have appeared to influence the work reported in this paper.

Acknowledgements

This research was funded by the Fondation des Gueules Cassées. We are grateful to A. Moisan (Cell Therapy and Engineering Unit, EFS Auvergne-Rhône-Alpes, Saint Ismier, France) for providing us with MSC. The Optimal small animal imaging platform is supported by France Life Imaging (French program "Investissement d'Avenir" grant; "Infrastructure d'avenir en Biologie Santé", ANR-11-INBS-0006) and the IBISA French consortium "Infrastructures en Biologie Santé et Agronomie". Some illustrations in this manuscript were created in BioRender and are published under a Biorender license (Ziegelmeyer, T. (2025) https://BioRender.com/u31z785).

Appendix A. Supplementary data

Supplementary data to this article can be found online at https://doi.org/10.1016/j.mtbio.2025.101710.

Data availability

Data will be made available on request.

References

[1] Z. Khatoon, C.D. McTiernan, E.J. Suuronen, T.-F. Mah, E.I. Alarcon, Bacterial biofilm formation on implantable devices and approaches to its treatment and prevention, Heliyon 4 (2018) e01067, https://doi.org/10.1016/j.heliyon.2018.e01067.

[2] M. Ribeiro, F.J. Monteiro, M.P. Ferraz, Infection of orthopedic implants with emphasis on bacterial adhesion process and techniques used in studying bacterial-material interactions, Biomatter 2 (2012) 176–194, https://doi.org/10.4161/biom.22905.

[3] A. Trampuz, A.F. Widmer, Infections associated with orthopedic implants, Curr. Opin. Infect. Dis. 19 (2006) 349–356, https://doi.org/10.1097/01.qco.0000235161.85925.e8.

[4] Y. Cui, H. Liu, Y. Tian, Y. Fan, S. Li, G. Wang, Y. Wang, C. Peng, D. Wu, Dual-functional composite scaffolds for inhibiting infection and promoting bone regeneration, Materials Today Bio 16 (2022) 100409, https://doi.org/10.1016/j.mtbio.2022.100409.

[5] B. Skerlavaj, G. Boix-Lemonche, The potential of surface-immobilized antimicrobial peptides for the enhancement of orthopaedic medical devices: a review, Antibiotics (Basel) 12 (2023) 211, https://doi.org/10.3390/antibiotics12020211.

[6] Antimicrobial and host-defense peptides as new anti-infective therapeutic strategies, in: R.E.W. Hancock, H.G. Sahl (Eds.), Nat. Biotechnol, vol. 24, 2006, pp. 1551–1557.

[7] S. Sang, S. Wang, C. Yang, Z. Geng, X. Zhang, Sponge-inspired sulfonated polyetheretherketone loaded with polydopamine-protected osthole nanoparticles and berberine enhances osteogenic activity and prevents implant-related infections, Chem. Eng. J. 437 (2022) 135255, https://doi.org/10.1016/j.cej.2022.135255.

[8] L. Zhao, P.K. Chu, Y. Zhang, Z. Wu, Antibacterial coatings on titanium implants, J. Biomed. Mater. Res. B Appl. Biomater. 91 (2009) 470–480.

[9] A. Tiwari, P. Sharma, B. Vishwamitra, G. Singh, Review on surface treatment for implant infection via gentamicin and antibiotic releasing coatings, Coatings 11 (2021) 1006.

[10] V. Allizond, S. Comini, A.M. Cuffini, G. Banche, Current knowledge on biomaterials for orthopedic applications modified to reduce bacterial adhesive ability, Antibiotics 11 (2022) 529, https://doi.org/10.3390/antibiotics11040529.

[11] S.H. Nguyen, H.K. Webb, R.J. Crawford, E.P. Ivanova, Natural antibacterial surfaces, in: E. Ivanova, R. Crawford (Eds.), Antibacterial Surfaces, Springer International Publishing, Cham, 2015, pp. 9–26, https://doi.org/10.1007/978-3-319-18594-1_2.

[12] D.P. Linklater, V.A. Baulin, S. Juodkazis, R.J. Crawford, P. Stoodley, E.P. Ivanova, Mechano-bactericidal actions of nanostructured surfaces, Nat. Rev. Microbiol. 19 (2021) 8–22, https://doi.org/10.1038/s41579-020-0414-z.

[13] A. Elbourne, R.J. Crawford, E.P. Ivanova, Nano-structured antimicrobial surfaces: from nature to synthetic analogues, J. Colloid Interface Sci. 508 (2017) 603–616, https://doi.org/10.1016/j.jcis.2017.07.021.

[14] C.M. Bhadra, V.K. Truong, V.T.H. Pham, M. Al Kobaisi, G. Seniutinas, J.Y. Wang, S. Juodkazis, R.J. Crawford, E.P. Ivanova, Antibacterial titanium nano-patterned arrays inspired by dragonfly wings, Sci. Rep. 5 (2015) 16817, https://doi.org/10.1038/srep16817.

[15] H. Shahali, J. Hasan, A. Mathews, H. Wang, C. Yan, T. Tesfamichael, P.K.D.V. Yarlagadda, Multi-biofunctional properties of three species of cicada wings and biomimetic fabrication of nanopatterned titanium pillars J, Mater. Chem. B 7 (2019) 1300–1310.

[16] L.E. Fisher, Y. Yang, M.F. Yuen, W. Zhang, A.H. Nobbs, B. Su, Bactericidal activity of biomimetic diamond nanocone surfaces, Biointerphases 11 (1) (2016) 011014, https://doi.org/10.1116/1.4944062, 17.

[17] M.N. Dickson, E.I. Liang, L.A. Rodriguez, N. Vollereaux, A.F. Yee, Nanopatterned polymer surfaces with bactericidal properties, Biointerphases 10 (2) (2015) 021010, https://doi.org/10.1116/1.4922157, 15.

[18] Y. Cheng, X. Ma, T. Franklin, R. Yang, C.I. Moraru, Mechano-bactericidal surfaces: mechanisms, nanofabrication, and prospects for food applications, Annu. Rev. Food Sci. Technol. 14 (2023) 449–472, https://doi.org/10.1146/annurev-food-060721-022330.

[19] S. Mo, K. Tang, Q. Liao, L. Xie, Y. Wu, G. Wang, Q. Ruan, A. Gao, Y. Lv, K. Cai, L. Tong, Z. Wu, P.K. Chu, H. Wang, Tuning the arrangement of lamellar nanostructures: achieving the dual function of physically killing bacteria and promoting osteogenesis, Mater. Horiz. 10 (2023) 881–888, https://doi.org/10.1039/D2MH01147F.

[20] E.P. Ivanova, D.P. Linklater, M. Werner, V.A. Baulin, X. Xu, N. Vrancken, S. Rubanov, E. Hanssen, J. Wandiyanto, V.K. Truong, A. Elbourne, S. Maclaughlin, S. Juodkazis, R.J. Crawford, The multi-faceted mechano-bactericidal mechanism of nanostructured surfaces, Proc. Natl. Acad. Sci. USA 117 (2020) 12598–12605, https://doi.org/10.1073/pnas.1916680117.

[21] F. Batool, H. Özçelik, C. Stutz, P.-Y. Gegout, N. Benkirane-Jessel, C. Petit, O. Huck, Modulation of immune-inflammatory responses through surface modifications of biomaterials to promote bone healing and regeneration, J. Tissue Eng. 12 (2021) 20417314211041428, https://doi.org/10.1177/20417314211041428.

[22] R. Whitaker, B. Hernaez-Estrada, R.M. Hernandez, E. Santos-Vizcaino, K. L. Spiller, Immunomodulatory biomaterials for tissue repair, Chem. Rev. 121 (2021) 11305–11335, https://doi.org/10.1021/acs.chemrev.0c00895.

[23] Z. Song, Y. Cheng, M. Chen, X. Xie, Macrophage polarization in bone implant repair: a review, Tissue Cell 82 (2023) 102112, https://doi.org/10.1016/j.tice.2023.102112.

[24] A.J. Rao, E. Gibon, T. Ma, Z. Yao, R.L. Smith, S.B. Goodman, Revision joint replacement, wear particles, and macrophage polarization, Acta Biomater. 8 (2012) 2815–2823, https://doi.org/10.1016/j.actbio.2012.03.042.

[25] S. Fan, X. Sun, C. Su, Y. Xue, X. Song, R. Deng, Macrophages—bone marrow mesenchymal stem cells crosstalk in bone healing, Front. Cell Dev. Biol. 11 (2023) 1193765, https://doi.org/10.3389/fcell.2023.1193765.

[26] F. Gong, T. Groth, C. Tu, M. Zhao, X. Huang, J. Chu, Crosstalk between macrophages and mesenchymal stem cells regulated by biomaterials and its role in bone regeneration, Adv. Mater. Sci. Eng. 2021 (2021) 9954205, https://doi.org/10.1155/2021/9954205.

[27] B. Huang, W. Wang, Q. Li, Z. Wang, B. Yan, Z. Zhang, L. Wang, M. Huang, C. Jia, J. Lu, S. Liu, H. Chen, M. Li, D. Cai, Y. Jiang, D. Jin, X. Bai, Osteoblasts secrete Cxcl9 to regulate angiogenesis in bone, Nat. Commun. 7 (2016) 13885, https://doi.org/10.1038/ncomms13885.

[28] H. Rosado-Galindo, M. Domenech, Substrate topographies modulate the secretory activity of human bone marrow mesenchymal stem cells, Stem Cell Res. Ther. 14 (2023) 208, https://doi.org/10.1186/s13287-023-03450-0.

[29] R.J. Miron, M. Bohner, Y. Zhang, D.D. Bosshardt, Osteoinduction and osteoimmunology: emerging concepts, Periodontology 94 (2024) (2000) 9–26, https://doi.org/10.1111/prd.12519.

[30] Y. Xie, C. Hu, Y. Feng, D. Li, T. Ai, Y. Huang, X. Chen, L. Huang, J. Tan, Osteoimmunomodulatory effects of biomaterial modification strategies on macrophage polarization and bone regeneration, Regen Biomater 7 (2020) 233–245, https://doi.org/10.1093/rb/rbaa006.

[31] L. Bai, P. Chen, Y. Zhao, R. Hang, X. Yao, B. Tang, C. Liu, Y. Xiao, R. Hang, A micro/nano-biomimetic coating on titanium orchestrates osteo/angio-genesis and osteoimmunomodulation for advanced osseointegration, Biomaterials 278 (2021) 121162, https://doi.org/10.1016/j.biomaterials.2021.121162.

[32] H.P. Jennissen, A macrophage model of osseointegration, Current Directions in Biomedical Engineering 2 (2016) 53–56, https://doi.org/10.1515/cdbme-2016-0015.

[33] S.N. Christo, The role of surface nanotopography and chemistry on primary neutrophil and macrophage cellular responses, Adv. Healthc. Mater 5 (2016) 956–965.

[34] Z. Geng, X. Li, L. Ji, Z. Li, Z. Cui, J. Wang, J. Cui, X. Yang, C. Liu, A novel snail-inspired bionic design of titanium with strontium-substituted hydroxyapatite coating for promoting osseointegration, Journal of Materials Sciences and Technology 79 (2020) 35, https://doi.org/10.1016/j.jmst.2020.11.041.

[35] S. Shirazi, S. Ravindran, L.F. Cooper, Topography-mediated immunomodulation in osseointegration; ally or enemy, Biomaterials 291 (2022) 121903, https://doi.org/10.1016/j.biomaterials.2022.121903.

[36] M.B. Berger, P. Slosar, Z. Schwartz, D.J. Cohen, S.B. Goodman, P.A. Anderson, B. D. Boyan, A review of biomimetic topographies and their role in promoting bone formation and osseointegration: implications for clinical use, Biomimetics 7 (2022) 46, https://doi.org/10.3390/biomimetics7020046.

[37] X. Li, Q. Huang, T.A. Elkhooly, Y. Liu, H. Wu, Q. Feng, L. Liu, Y. Fang, W. Zhu, T. Hu, Effects of titanium surface roughness on the mediation of osteogenesis via modulating the immune response of macrophages, Biomed. Mater. 13 (2018) 045013, https://doi.org/10.1088/1748-605X/aabe33.

[38] L.O. Bailey, S. Lippiatt, F.S. Biancanello, S.D. Ridder, N.R. Washburn, The quantification of cellular viability and inflammatory response to stainless steel

alloys, Biomaterials 26 (2005) 5296–5302, https://doi.org/10.1016/j.biomaterials.2005.01.055.
[39] T.L. Clainche, D. Linklater, S. Wong, P. Le, S. Juodkazis, X.L. Guével, J.-L. Coll, E. P. Ivanova, V. Martel-Frachet, Mechano-bactericidal titanium surfaces for bone tissue engineering, ACS Appl. Mater. Interfaces 12 (2020) 48272–48283, https://doi.org/10.1021/acsami.0c11502.
[40] W. Teughels, N. Van Assche, I. Sliepen, M. Quirynen, Effect of material characteristics and/or surface topography on biofilm development, Clinical Oral Implants Research 17 (2006) 68–81, https://doi.org/10.1111/j.1600-0501.2006.01353.x.
[41] J.V. Wandiyanto, T. Tamanna, D.P. Linklater, V.K. Truong, M. Al Kobaisi, V. A. Baulin, S. Joudkazis, H. Thissen, R.J. Crawford, E.P. Ivanova, Tunable morphological changes of asymmetric titanium nanosheets with bactericidal properties, J. Colloid Interface Sci. 560 (2020) 572–580, https://doi.org/10.1016/j.jcis.2019.10.067.
[42] M.B. Berger, P. Slosar, Z. Schwartz, D.J. Cohen, S.B. Goodman, P.A. Anderson, B. D. Boyan, A review of biomimetic topographies and their role in promoting bone formation and osseointegration: implications for clinical use, Biomimetics 7 (2022) 46, https://doi.org/10.3390/biomimetics7020046.
[43] V. Goriainov, G. Hulsart-Billstrom, T. Sjostrom, D.G. Dunlop, B. Su, R.O.C. Oreffo, Harnessing nanotopography to enhance osseointegration of clinical orthopedic titanium implants—an in vitro and in vivo analysis, Front. Bioeng. Biotechnol. 6 (2018) 44, https://doi.org/10.3389/fbioe.2018.00044.
[44] J.V. Wandiyanto, S. Cheeseman, V.K. Truong, M.A. Kobaisi, C. Bizet, S. Juodkazis, H. Thissen, R.J. Crawford, E.P. Ivanova, Outsmarting superbugs: bactericidal activity of nanostructured titanium surfaces against methicillin- and gentamicin-resistant Staphylococcus aureus ATCC 33592, J. Mater. Chem. B 7 (2019) 4424–4431, https://doi.org/10.1039/C9TB00102F.
[45] International Organization Standardization, Measurement of antibacterial activity on plastics and other non-porous surfaces. https://www.iso.org/standard/54431.html, 2011.
[46] R.M. Sabino, K.C. Popat, Evaluating whole blood clotting in vitro on biomaterial surfaces, Bio Protoc 10 (2020) e3505, https://doi.org/10.21769/BioProtoc.3505.
[47] V.K. Manivasagam, K.C. Popat, In vitro investigation of hemocompatibility of hydrothermally treated titanium and titanium alloy surfaces, ACS Omega 5 (2020) 8108–8120, https://doi.org/10.1021/acsomega.0c00281.
[48] H. Chen, C. Wang, X. Yang, Z. Xiao, X. Zhu, K. Zhang, Y. Fan, X. Zhang, Construction of surface HA/TiO2 coating on porous titanium scaffolds and its preliminary biological evaluation, Mater. Sci. Eng. C 70 (2017) 1047–1056, https://doi.org/10.1016/j.msec.2016.04.013.
[49] E. Saino, V. Maliardi, E. Quartarone, L. Fassina, L. Benedetti, M.G.C. De Angelis, P. Mustarelli, A. Facchini, L. Visai, In vitro enhancement of SAOS-2 cell calcified matrix deposition onto radio frequency magnetron sputtered bioglass-coated titanium scaffolds, Tissue Eng Part A 16 (2010) 995–1008, https://doi.org/10.1089/ten.TEA.2009.0051.
[50] T. Taguchi, M.J. Lopez, An overview of de novo bone generation in animal models, J. Orthop. Res. 39 (2021) 7–21, https://doi.org/10.1002/jor.24852.
[51] P.P. Spicer, J.D. Kretlow, S. Young, J.A. Jansen, F.K. Kasper, A.G. Mikos, Evaluation of bone regeneration using the rat critical size calvarial defect, Nat. Protoc. 7 (2012) 1918–1929, https://doi.org/10.1038/nprot.2012.113.
[52] C. Kunert-Keil, H. Richter, I. Zeidler-Rentzsch, I. Bleeker, T. Gredes, Histological comparison between laser microtome sections and ground specimens of implant-containing tissues, Annals of Anatomy - Anatomischer Anzeiger 222 (2019) 153–157, https://doi.org/10.1016/j.aanat.2018.12.001.
[53] S.P. Mitra, Protein adsorption on biomaterial surfaces: subsequent conformational and biological consequences – a review, jsst. https://doi.org/10.18311/jsst/2020/23282, 2020.
[54] K.M. Sousa, D.P. Linklater, V.A. Baulin, C. Dekiwadia, E. Mayes, B.J. Murdoch, P. H. Le, C.J. Fluke, V. Boshkovikj, C. Wen, R.J. Crawford, E.P. Ivanova, Understanding the influence of serum proteins adsorption on the mechano-bactericidal efficacy and immunomodulation of nanostructured titanium, Adv. Mater. Interfaces 11 (2024) 2301021, https://doi.org/10.1002/admi.202301021.
[55] D.H.K. Nguyen, V.T.H. Pham, M.A. Kobaisi, C. Bhadra, A. Orlowska, S. Ghanaati, B.M. Manzi, V.A. Baulin, S. Joudkazis, P. Kingshott, R.J. Crawford, E.P. Ivanova, Adsorption of human plasma albumin and fibronectin onto nanostructured black silicon surfaces, Langmuir 32 (2016) 10744.
[56] B.M. Manzi, M. Werner, E.P. Ivanova, R.J. Crawford, V.A. Baulin, Simulations of protein adsorption on nanostructured surfaces, Sci. Rep. 9 (2019) 4694.
[57] Z. Li, M.K. Delaney, K.A. O'Brien, X. Du, Signaling during platelet adhesion and activation, Arterioscler. Thromb. Vasc. Biol. 30 (2010) 2341–2349, https://doi.org/10.1161/ATVBAHA.110.207522.
[58] J.N. Barbosa, D.P. Vasconcelos, Chapter 3 - macrophage response to biomaterials, in: M. Mozafari (Ed.), Handbook of Biomaterials Biocompatibility, Woodhead Publishing, 2020, pp. 43–52, https://doi.org/10.1016/B978-0-08-102967-1.00003-7.
[59] J.M. Anderson, A. Rodriguez, D.T. Chang, Foreign body reaction to biomaterials, Semin. Immunol. 20 (2008) 86–100, https://doi.org/10.1016/j.smim.2007.11.004.
[60] K.E. Martin, A.J. García, Macrophage phenotypes in tissue repair and the foreign body response: implications for biomaterial-based regenerative medicine strategies, Acta Biomater. 133 (2021) 4–16, https://doi.org/10.1016/j.actbio.2021.03.038.
[61] A. Javed, J.-S. Bae, F. Afzal, S. Gutierrez, J. Pratap, S.K. Zaidi, Y. Lou, A.J. van Wijnen, J.L. Stein, G.S. Stein, J.B. Lian, Structural coupling of Smad and Runx2 for execution of the BMP2 osteogenic signal, J. Biol. Chem. 283 (2008) 8412–8422, https://doi.org/10.1074/jbc.M705578200.
[62] R.B. Kato, B. Roy, F.S. De Oliveira, E.P. Ferraz, P.T. De Oliveira, A.G. Kemper, M. Q. Hassan, A.L. Rosa, M.M. Beloti, Nanotopography directs mesenchymal stem cells to osteoblast lineage through regulation of microRNA-SMAD-BMP-2 circuit, J. Cell. Physiol. 229 (2014) 1690–1696, https://doi.org/10.1002/jcp.24614.
[63] H. Hanna, L.M. Mir, F.M. Andre, In vitro osteoblastic differentiation of mesenchymal stem cells generates cell layers with distinct properties, Stem Cell Res. Ther. 9 (2018) 203, https://doi.org/10.1186/s13287-018-0942-x.
[64] J. Si, C. Wang, D. Zhang, B. Wang, W. Hou, Y. Zhou, Osteopontin in bone metabolism and bone diseases, Med. Sci. Monit. 26 (2020) e919159, https://doi.org/10.12659/MSM.919159, 1-e919159-9.
[65] W. Chen, G. Xie, Y. Lu, J. Wang, B. Feng, Q. Wang, K. Xu, J. Bao, An improved osseointegration of metal implants by pitavastatin loaded multilayer films with osteogenic and angiogenic properties, Biomaterials 280 (2022) 121260, https://doi.org/10.1016/j.biomaterials.2021.121260.
[66] A.P. Kusumbe, S.K. Ramasamy, R.H. Adams, Coupling of angiogenesis and osteogenesis by a specific vessel subtype in bone, Nature 507 (2014) 323–328, https://doi.org/10.1038/nature13145.
[67] P.S. Gomes, M.H. Fernandes, Rodent models in bone-related research: the relevance of calvarial defects in the assessment of bone regeneration strategies, Lab Anim Jan 45 (1) (2011) 14–24.
[68] E. Roddy, M.R. DeBaun, A. Daoud-Gray, Y.P. Yang, M.J. Gardner, Treatment of critical-sized bone defects: clinical and tissue engineering perspectives, Eur J Orthop Surg Traumatol Apr 28 (3) (2018) 351–362, https://doi.org/10.1007/s00590-017-2063-0.
[69] L.P. Hatt, K. Thompson, J.A. Helms, M.J. Stoddart, A.R. Armiento, Clinically relevant preclinical animal models for testing novel cranio-maxillofacial bone 3D-printed biomaterials, Clin. Transl. Med. 12 (2022) e690, https://doi.org/10.1002/ctm2.690.
[70] N. Stoppie, J.P. Waerden, J.A. Jansen, J. Duyck, M. Wevers, I.E. Naert, Validation of microfocus computed tomography in the evaluation of bone implant specimens, Clin. Implant Dent. Relat. Res. 7 (2005) 87–94, https://doi.org/10.1111/j.1708-8208.2005.tb00051.x.
[71] H.J. Haugen, S.P. Lyngstadaas, F. Rossi, G. Perale, Bone grafts: which is the ideal biomaterial? J. Clin. Periodontol. 46 (2019) 92–102, https://doi.org/10.1111/jcpe.13058.
[72] D. Karazisis, L. Rasmusson, S. Petronis, A. Palmquist, F.A. Shah, H. Agheli, L. Emanuelsson, A. Johansson, O. Omar, P. Thomsen, The effects of controlled nanotopography, machined topography and their combination on molecular activities, bone formation and biomechanical stability during osseointegration, Acta Biomater. 136 (2021) 279–290, https://doi.org/10.1016/j.actbio.2021.10.001.
[73] A.A. T, A.-M. S, A. Ns, A. Aa, A. Am, A. Hs, B. Mk, A. Ba, A. N, Optimizing osseointegration in dental implantology: a cross-disciplinary review of current and emerging strategies, Cureus 15 (10) (2023) e47943, https://doi.org/10.7759/cureus.47943, 30.
[74] P. Jiang, Y. Zhang, R. Hu, B. Shi, L. Zhang, Q. Huang, Y. Yang, P. Tang, C. Lin, Advanced surface engineering of titanium materials for biomedical applications: from static modification to dynamic responsive regulation, Bioact. Mater. (2023), https://doi.org/10.1016/j.bioactmat.2023.03.006.
[75] A. Barfeie, J. Wilson, J. Rees, Implant surface characteristics and their effect on osseointegration, Br. Dent. J. 218 (5) (2015) E9, https://doi.org/10.1038/sj.bdj.2015.171, 13.
[76] E. Gongadze, D. Kabaso, S. Bauer, J. Park, P. Schmuki, A. Iglič, Adhesion of osteoblasts to a vertically aligned TiO2 nanotube surface, Mini Rev. Med. Chem. 13 (2013) 194–200.
[77] R.M. Visalakshan, M.N. MacGregor, S. Sasidharan, A. Ghazaryan, A. M. Mierczynska-Vasilev, S. Morsbach, V. Mailänder, K. Landfester, J.D. Hayball, K. Vasilev, Biomaterial surface hydrophobicity-mediated serum protein adsorption and immune responses, ACS Appl. Mater. Interfaces 11 (31) (2019 Aug 7) 27615–27623, https://doi.org/10.1021/acsami.9b09900, 2019.
[78] J. Yang, Y. Zhou, F. Wei, Y. Xiao, Blood clot formed on rough titanium surface induces early cell recruitment, Clin Oral Implant Res 27 (2016) 1031–1038, https://doi.org/10.1111/clr.12672.
[79] P.W. Kämmerer, M. Gabriel, B. Al-Nawas, T. Scholz, C.M. Kirchmaier, M.O. Klein, Early implant healing: promotion of platelet activation and cytokine release by topographical, chemical and biomimetical titanium surface modifications in vitro, Clin. Oral Implants Res. 23 (2012) 504–510, 10 1111 1600-0501 2011 02153.
[80] Q. Zhang, J.W. Hwang, J.-H. Oh, C.H. Park, S.H. Chung, Y.-S. Lee, J.-H. Baek, H.-M. Ryoo, K.M. Woo, Effects of the fibrous topography-mediated macrophage phenotype transition on the recruitment of mesenchymal stem cells: an *in vivo* study, Biomaterials 149 (2017) 77–87, https://doi.org/10.1016/j.biomaterials.2017.10.007.
[81] T.U. Luu, S.C. Gott, B.W.K. Woo, M.P. Rao, W.F. Liu, Micro- and nanopatterned topographical cues for regulating macrophage cell shape and phenotype, ACS Appl. Mater. Interfaces 7 (2015) 28665–28672, https://doi.org/10.1021/acsami.5b10589.
[82] J. Wang, F. Meng, W. Song, J. Jin, Q. Ma, D. Fei, L. Fang, L. Chen, Q. Wang, Y. Zhang, Nanostructured titanium regulates osseointegration via influencing macrophage polarization in the osteogenic environment, Int J Nanomedicine 13 (2018) 4029–4043, https://doi.org/10.2147/IJN.S163956.
[83] Y. Zhu, H. Liang, X. Liu, J. Wu, C. Yang, T.M. Wong, K.Y.H. Kwan, K.M.C. Cheung, S. Wu, K.W.K. Yeung, Regulation of macrophage polarization through surface topography design to facilitate implant-to-bone osteointegration, Sci. Adv. 2 (14) (2021) eabf6654, https://doi.org/10.1126/sciadv.abf6654, 7.

[84] Q.L. Ma, L.Z. Zhao, R.R. Liu, B.Q. Jin, W. Song, Y. Wang, Y.S. Zhang, L.H. Chen, Y. M. Zhang, Improved implant osseointegration of a nanostructured titanium surface via mediation of macrophage polarization, Biomaterials Dec 35 (37) (2014) 9853–9867, https://doi.org/10.1016/j.biomaterials.2014.08.025.
[85] K. Modaresifar, M. Ganjian, P.J. Díaz-Payno, M. Klimopoulou, M. Koedam, B.C. J. van der Eerden, L.E. Fratila-Apachitei, A.A. Zadpoor, Mechanotransduction in high aspect ratio nanostructured meta-biomaterials: the role of cell adhesion, contractility, and transcriptional factors, Materials Today Bio 16 (2022) 100448, https://doi.org/10.1016/j.mtbio.2022.100448.
[86] M.J. Dalby, N. Gadegaard, R.O.C. Oreffo, Harnessing nanotopography and integrin–matrix interactions to influence stem cell fate, Nature Mater 13 (2014) 558–569, https://doi.org/10.1038/nmat3980.
[87] Z. Huo, W. Yang, J. Harati, A. Nene, F. Borghi, C. Piazzoni, P. Milani, S. Guo, M. Galluzzi, D. Boraschi, Biomechanics of macrophages on disordered surface nanotopography, ACS Appl. Mater. Interfaces 16 (2024) 27164–27176, https://doi.org/10.1021/acsami.4c04330.
[88] A.T. Xu, Y.W. Xie, J.G. Xu, J. Li, H. Wang, F.M. He, Effects of strontium-incorporated micro/nano rough titanium surfaces on osseointegration via modulating polarization of macrophages, Colloids Surf. B Biointerfaces (2021), https://doi.org/10.1016/j.colsurfb.2021.111992.
[89] R.M. Visalakshan, R. Bright, A.L.S. Burzava, A.J. Barker, J. Simon, N. Ninan, D. Palms, J. Wood, M. Martínez-Negro, S. Morsbach, V. Mailänder, P. H. Anderson, T. Brown, D. Barker, K. Landfester, K. Vasilev, Antibacterial nanostructured surfaces modulate protein adsorption, inflammatory responses, and fibrous capsule formation, ACS Appl. Mater. Interfaces 11 (1) (2023) 220–235, https://doi.org/10.1021/acsami.2c13415, 15.
[90] H. Pan, Y. Xie, Z. Zhang, K. Li, D. Hu, X. Zheng, T. Tang, Immunomodulation effect of a hierarchical macropore/nanosurface on osteogenesis and angiogenesis, Biomed. Mater. 12 (2017) 045006, https://doi.org/10.1088/1748-605X/aa6b7c.
[91] K. Li, L. Lv, D. Shao, Y. Xie, Y. Cao, X. Zheng, Engineering nanopatterned structures to orchestrate macrophage phenotype by cell shape, J. Funct. Biomater. 13 (2022) 31, https://doi.org/10.3390/jfb13010031.
[92] K. Martins de Sousa, D.P. Linklater, V.A. Baulin, C. Dekiwadia, E. Mayes, B. J. Murdoch, P.H. Le, C.J. Fluke, V. Boshkovikj, C. Wen, R.J. Crawford, E. P. Ivanova, Understanding the influence of serum proteins adsorption on the mechano-bactericidal efficacy and immunomodulation of nanostructured titanium, Adv. Mater. Interfac. 11 (2024) 2301021, https://doi.org/10.1002/admi.202301021.
[93] N. Kartikasari, M. Yamada, J. Watanabe, W. Tiskratok, X. He, H. Egusa, Titania nanospikes activate macrophage phagocytosis by ligand-independent contact stimulation, Sci. Rep. 12 (2022) 12250, https://doi.org/10.1038/s41598-022-16214-2.
[94] Y. Chen, L. Zhou, M. Guan, S. Jin, P. Tan, X. Fu, Z. Zhou, Multifunctionally disordered TiO2 nanoneedles prevent periprosthetic infection and enhance osteointegration by killing bacteria and modulating the osteoimmune microenvironment, Theranostics 14 (2024) 6016–6035, https://doi.org/10.7150/thno.98219.
[95] R. Bright, D. Fernandes, J. Wood, D. Palms, A. Burzava, N. Ninan, T. Brown, D. Barker, K. Vasilev, Long-term antibacterial properties of a nanostructured titanium alloy surface: an in vitro study, Mater Today Bio 13 (2022) 100176, https://doi.org/10.1016/j.mtbio.2021.100176.
[96] S. Dobbenga, L.E. Fratila-Apachitei, A.A. Zadpoor, Nanopattern-induced osteogenic differentiation of stem cells – a systematic review, Acta Biomater. 46 (2016) 3–14, https://doi.org/10.1016/j.actbio.2016.09.031.
[97] W. Yang, W. Han, W. He, J. Li, J. Wang, H. Feng, Y. Qian, Surface topography of hydroxyapatite promotes osteogenic differentiation of human bone marrow mesenchymal stem cells, Mater. Sci. Eng. C 60 (2016) 45–53, https://doi.org/10.1016/j.msec.2015.11.012.
[98] A.A. Bertrand, S.H. Malapati, D.T. Yamaguchi, J.C. Lee, The intersection of mechanotransduction and regenerative osteogenic materials, Adv. Healthcare Mater. 9 (2020) 2000709, https://doi.org/10.1002/adhm.202000709.
[99] Z. Geng, Z. Li, Z. Cui, J. Wang, X. Yang, C. Liu, Novel bionic topography with MiR-21 coating for improving bone-implant integration through regulating cell adhesion and angiogenesis, Nano Lett. 20 (2020) 7716–7721, https://doi.org/10.1021/acs.nanolett.0c03240.
[100] Q. Ma, L. Fang, N. Jiang, L. Zhang, Y. Wang, Y. Zhang, L. Chen, Bone mesenchymal stem cell secretion of sRANKL/OPG/M-CSF in response to macrophage-mediated inflammatory response influences osteogenesis on nanostructured Ti surfaces, Biomaterials 154 (2018) 234–247, https://doi.org/10.1016/j.biomaterials.2017.11.003.
[101] F. Viela, D. Granados, A. Ayuso-Sacido, I. Rodríguez, Mechanobiology: biomechanical cell regulation by high aspect ratio nanoimprinted pillars, Adv. Funct. Mater. 31/2016), Advanced Functional Materials 26 (2016), https://doi.org/10.1002/adfm.201670199, 5582–5582.
[102] L.E. Dickinson, D.R. Rand, J. Tsao, W. Eberle, S. Gerecht, Endothelial cell responses to micropillar substrates of varying dimensions and stiffness, J. Biomed. Mater. Res. 100 (2012) 1457–1466, https://doi.org/10.1002/jbm.a.34059.
[103] C.M. Champagne, J. Takebe, S. Offenbacher, L.F. Cooper, Macrophage cell lines produce osteoinductive signals that include bone morphogenetic protein-2, Bone 30 (2002) 26–31, https://doi.org/10.1016/S8756-3282(01)00638-X.
[104] G. Pan, S. Sun, W. Zhang, R. Zhao, W. Cui, F. He, L. Huang, S.-H. Lee, K.J. Shea, Q. Shi, H. Yang, Biomimetic design of mussel-derived bioactive peptides for dual-functionalization of titanium-based biomaterials, J. Am. Chem. Soc. 138 (2016) 15078–15086, https://doi.org/10.1021/jacs.6b09770.
[105] Z. Liu, H. Ding, L. Qi, J. Wang, Y. Li, L. Liu, G. Feng, L. Zhang, Core-shell NiS@SrTiO3 nanorods on titanium for enhanced osseointegration via programmed regulation of bacterial infection, angiogenesis, and osteogenesis, ACS Appl. Mater. Interfaces (2023), https://doi.org/10.1021/acsami.3c11995.